PREDICTIVE UNCERTAINTY QUANTIFICATION FOR BIRD'S EYE VIEW SEGMENTATION: A BENCHMARK AND NOVEL LOSS FUNCTION

Anonymous authors
Paper under double-blind review

ABSTRACT

The fusion of raw sensor data to create a Bird's Eye View (BEV) representation is critical for autonomous vehicle planning and control. Despite the growing interest in using deep learning models for BEV semantic segmentation, anticipating segmentation errors and enhancing the explainability of these models remain under-explored. This paper introduces a comprehensive benchmark for predictive uncertainty quantification in BEV segmentation, evaluating multiple approaches across three popular datasets and two representative backbones. Our study focuses on the effectiveness of the quantified uncertainty in detecting misclassified and out-of-distribution (OOD) pixels, while also improving model calibration. Through empirical analysis, we uncover challenges in existing uncertainty quantification methods and demonstrate the potential of evidential deep learning techniques, which capture both aleatoric and epistemic uncertainty. To address these challenges, we propose a novel loss function, Uncertainty-Focal-Cross-Entropy (UFCE), specifically designed for highly imbalanced data, along with a simple uncertainty-scaling regularization term that improve both uncertainty quantification and model calibration for BEV segmentation [1].

1 INTRODUCTION

Bird's Eye View (BEV) semantic segmentation is a critical component of modern vehicular technology and has received increased attention in recent years. It has been adopted in advanced autonomous vehicle systems, such as Tesla's Autopilot. BEV representations offer a top-down perspective of the environment surrounding a vehicle, created by fusing data from multiple sensors such as cameras, LiDAR, and radar (Philion & Fidler, 2020). This comprehensive view allows autonomous systems to accurately perceive the position and movement of nearby objects, including other vehicles, pedestrians, and obstacles. Therefore, BEV semantic segmentation (BEVSS) plays a vital role in both autonomous driving systems and advanced driver-assistance systems (ADAS) (Liu et al., 2023)

Identifying potential errors before they lead to dangerous outcomes is crucial for ensuring the safety and reliability of BEV semantic segmentation. However, Deep Neural Networks (DNNs) commonly used for BEV representation learning tend to make overconfident predictions on unseen data (Guo et al., 2017) and underconfident predictions on noisy data (Wang et al., 2021). In March 2018, an Uber autonomous vehicle in Arizona, failed to correctly identify a pedestrian crossing outside a designated crosswalk at night, resulting in a fatal collision (Goodman, 2018). In March 2022, a Tesla Model S on Autopilot crashed into a stationary vehicle on a Florida highway, injuring five police officers (Shepardson, 2022).

Uncertainty prediction in segmentation can enable autonomous systems to return control to the driver when necessary. There are two primary types of uncertainty (Kendall & Gal, 2017). *Aleatoric uncertainty*, which arises from inherent randomnesses, such as noisy data and labels. By identifying areas with high aleatoric uncertainty, the vehicle can make better decisions, especially in complex or ambiguous situations. *Epistemic uncertainty*, on the other hand, stems from a lack of knowledge, such as when the test-time input differs significantly from the training data. Quantifying epistemic

[1] The code is available at https://anonymous.4open.science/r/ubev-E357/

uncertainty helps the system handle out-of-distribution scenarios and adapt to unexpected conditions, especially in dynamic driving environments.

Uncertainty quantification methods can be broadly categorized based on their computational complexity and approach. The first category involves multiple forward passes to estimate a model's predictive uncertainty, including methods such as deep ensembles (Lakshminarayanan et al., 2017) and dropout-based approaches (Gal & Ghahramani, 2016). While effective, these methods are computationally expensive, making them impractical for real-time applications. The second category utilizes deterministic single forward-pass neural networks. Conjugate-prior-based methods, like evidential neural networks (Sensoy et al., 2018), predict a conjugate prior distribution of class probabilities, providing multi-dimensional uncertainty estimates. Additionally, post-hoc methods, such as those based on softmax (Hendrycks & Gimpel, 2016) and energy models (Liu et al., 2020), are notable for their ease of adoption without requiring modifications to the underlying network architecture,

This study investigates the uncertainty-aware BEVSS task, which involves pixel-level classification in the BEV view while estimating the associated uncertainties. Our main contributions are:

- We introduce the first benchmark for evaluating uncertainty quantification methods in BEVSS, analyzing five representative approaches (softmax entropy, energy, deep ensemble, dropout, and evidential) across three popular datasets (CARLA (Dosovitskiy et al., 2017), nuScenes (Caesar et al., 2020), and Lyft (Kesten et al., 2019)) using two BEVSS backbones (Lift-Splat-Shoot (Philion & Fidler, 2020) and Cross-View-Transformer (Zhou & Krähenbühl, 2022)).
- We propose the UFCE loss, which we theoretically demonstrate can implicitly regularize sample weights, mitigating both under-fitting and over-fitting. Additionally, we introduce a simple uncertainty-scaling regularization term that explicitly adjusts sample weights based on epistemic uncertainty.
- Extensive experiments demonstrate that our proposed framework consistently achieves the best epistemic uncertainty estimation, improving the AUPR for OOD detection by an average of 4.758% over the runner-up model. Additionally, it delivers top-tier aleatoric uncertainty performance, as evaluated through calibration and misclassification detection, all while maintaining high segmentation accuracy.

2 Uncertainty Quantification on BEVSS

Problem Formulation: Suppose we are given n images from RGB camera views surrounding the ego vehicle. Let $\mathbf{X} := \{\mathbf{X}_k, \mathbf{E}_k, \mathbf{I}_k\}_{k=1}^{n}$ denote the input, where each camera view has a feature matrix $\mathbf{X}_k \in \mathbb{R}^{3\times H\times W}$ (with H and W representing the height and width of the input image), an extrinsic matrix $\mathbf{E}_k \in \mathbb{R}^{3\times 4}$, and an intrinsic matrix $\mathbf{I}_k \in \mathbb{R}^{3\times 3}$. Uncertainty-aware BEV semantic segmentation aims to predict pixel-level classes in the BEV coordinate frame, represented by $\mathbf{Y} \in \{0,1\}^{C\times M\times N}$, along with the aleatoric uncertainty $u_{i,j}^{alea}$ and epistemic uncertainty $u_{i,j}^{epis}$. Here, C denotes the number of classes, while M and N represent the width and height of the BEV frame, respectively.

A common BEVSS neural network has the general form:

$$\mathbf{P} = \sigma_{\text{softmax}}\left(f(\mathbf{X};\boldsymbol{\theta})\right), \tag{1}$$

where $\mathbf{P} \in [0,1]^{C\times M\times N}$ are the pixel-wise class probabilities, and $\boldsymbol{\theta}$ refers to the network parameters. We use $\mathbf{p}_{i,j}$ to denote the class-probability vector of the BEV pixel at index (i,j).

Benchmark Setting: In this benchmark, we aim to investigate the performance of various uncertainty quantification methods on the uncertainty-aware BEVSS task. We consider two BEVSS frameworks as the backbone: Lift-Splat-Shoot (LSS) (Philion & Fidler, 2020) and Cross-View Transformer (CVT) (Zhou & Krähenbühl, 2022). LSS lifts 2D camera images into a 3D space, projects them onto a BEV plane, and then processes the BEV features for semantic segmentation. CVT, on the other hand, leverages attention mechanisms to transform multi-view image inputs into a unified BEV representation, enabling more effective cross-view feature fusion. Details of the models are provided in Appendix A.2.1.

We apply five representative uncertainty quantification methods, originally designed for independent inputs such as image-level classification. One widely used metric is *entropy* (Hendrycks & Gimpel,

2016), which is known to capture aleatoric uncertainty for in-distribution samples and is preferred by its simplicity and lack of computational overhead. Additionally, Liu et al. (2020) proposed the use of an *energy* score to distinguish between in-distribution and out-of-distribution samples, which is also a post-hoc method. We also consider the *ensemble-based* method (Lakshminarayanan et al., 2017), which estimates uncertainty by training multiple models and averaging their predictions. Similarly, the *dropout-based* method (Gal & Ghahramani, 2016) approximates Bayesian inference by performing dropout during inference. These two methods generate multiple class probability predictions and the variance is used as uncertainty metric. These four methods do not require significant architectural changes to the network. Detailed descriptions of the models and uncertainty calculations are presented in Appendix A.2.3. Lastly, the *evidential neural network (ENN)* (Sensoy et al., 2018) replaces the standard softmax activation with ReLU function and produces the multinomial opinions in subjective logic. While this approach modifies the model architecture, it requires only a single training pass to generate both aleatoric and epistemic uncertainty, along with the class probabilities.

Evidential Neural Networks (ENN): Due to computational efficiency and explainability, we extend ENNs to conduct uncertainty quantification for BEVSS, where pixel-level prediction is expected. We adapt the BEVSS network architecture (LSS or CVT) and replace the last softmax activation function with the ReLU activation function to predict parameters of a non-degenerate Dirichlet distribution.

$$\mathbf{A} = \sigma_{\text{ReLU}}\left(f(\mathbf{X};\boldsymbol{\theta})\right) + \mathbf{1}, \mathbf{A} \in \mathbb{R}^{+^{C\times M\times N}} \tag{2}$$

Considering the conjunction relation between the Dirichlet distribution and Categorical distribution, the class label follows a categorical distribution parameterized by $\boldsymbol{p}_{i,j}$, which itself follows a Dirichlet distribution parameterized by $\boldsymbol{\alpha}_{i,j} := \mathbf{A}[:,i,j]$. We omit the index (i,j) in the subsequent discussion for simplicity.

$$\boldsymbol{y} \sim \text{Cat}(\boldsymbol{y}|\mathbf{p}),\ \mathbf{p} \sim \text{Dir}(\boldsymbol{p}|\boldsymbol{\alpha}), \tag{3}$$

The expected class probability can be derived as shown in Equation 4, where $\alpha_0 = \sum_{c=1}^{C} \alpha_c$:

$$\bar{\mathbf{p}} := \mathbb{E}[\mathbf{p}|\boldsymbol{\alpha}] = \boldsymbol{\alpha}/\alpha_0 \tag{4}$$

Based on subjective logic opinion (Jøsang, 2016), there is a bijection between subjective opinions and Dirichlet PDFs, allowing a C-dimensional Dirichlet probability distribution to represent a multinomial opinion. Intuitively, we introduce the concept of "evidence", defined as a metric indicating the volume of supportive observations gathered from training data which suggests a sample belongs to a specific class. Let $e_c \geq 0$ represent the evidence for class c, with $e_c = \alpha_c - 1$. Higher evidence demonstrates stronger confidence in classifying a sample into the corresponding category, whereas lower overall evidence across all classes suggests a lack of similarity with the training data, indicating a higher likelihood of the sample being out-of-distribution.

Then we discuss the optimization loss for evidential-based models. UCE loss associated with an entropy regularizer is commonly used in evidential-based models (Sensoy et al., 2018; Charpentier et al., 2020), With a training dataset $\mathcal{D}^{train}$,

$$\mathcal{L}^{\text{UCE-ENT}}(\boldsymbol{\theta}) = \mathbb{E}_{(\boldsymbol{X},\boldsymbol{y})\sim\mathcal{D}^{train}}\left[\mathcal{L}^{\text{UCE}}\left(\boldsymbol{\theta},\boldsymbol{X},\boldsymbol{y}\right) - \beta\mathcal{L}^{\text{ENT}}(\boldsymbol{\theta},\boldsymbol{X})\right] \tag{5}$$

The first component, called UCE loss, aims to minimize the expected cross-entropy loss between the predicted class probabilities and the target categorical distribution. Here, the predicted categorical distribution is derived from the anticipated Dirichlet distribution, while the target distribution follows a one-hot encoding format. This approach strengthens the evidential support for the true class while reducing support for other classes.

$$\mathcal{L}^{\text{UCE}}\left(\boldsymbol{\theta},\boldsymbol{X},\boldsymbol{y}\right) = \mathbb{E}_{\boldsymbol{p}\sim\text{Dir}(\boldsymbol{\alpha}(\boldsymbol{\theta},\boldsymbol{X}))}\left[\mathbb{H}\left(\boldsymbol{p},\boldsymbol{y}\right)\right] = \sum_{c=1}^{C} y_c\left(\psi(\alpha_0) - \psi(\alpha_c)\right)$$

The second component, termed the Entropy Regularizer (ER), involves the entropy of the predicted Dirichlet distribution. This can be viewed as the Kullback-Leibler (KL) divergence between the predicted Dirichlet distribution and a uniform Dirichlet prior, promoting a smooth Dirichlet distribution. The closed-form of the Bayesian loss is provided in Appendix A.1.

$$\mathcal{L}^{\text{ENT}}(\boldsymbol{\theta},\boldsymbol{X}) = \mathbb{H}\left(\text{Dir}\left(\boldsymbol{\alpha}(\boldsymbol{\theta},\boldsymbol{X})\right)\right) = \text{KL}\left(\text{Dir}(\boldsymbol{p}|\boldsymbol{\alpha}(\boldsymbol{\theta},\boldsymbol{X}))\parallel\text{Dir}(\boldsymbol{p}|\mathbf{1})\right)$$

3 METHODOLOGY

In this section, we begin by discussing the limitations of the commonly used UCE loss for ENN models in Section 3.1. Next, we formally introduce our proposed UFCE loss in Section 3.2, highlighting how it partially addresses the limitations of UCE. Finally, we present our proposed uncertainty quantification framework in Section 3.3.

3.1 LIMITAION OF UCE

In an uncertainty-aware classification task, there are three levels of ground-truth and prediction comparisons:

1. A one-hot encoded classification label, denoted as ground truth $\hat{\boldsymbol{y}}$, compared to the predicted label $\boldsymbol{y}$.
2. A ground-truth categorical distribution $\text{Cat}(\hat{\boldsymbol{p}})$ aligned with the predicted expected categorical distribution $\text{Cat}(\boldsymbol{p})$ from an evidential neural network (ENN). Gathering soft labels maybe resource-intensive and susceptible to noise.
3. A ground-truth distribution over the categorical distribution $\text{Dir}(\hat{\boldsymbol{\alpha}})$, compared to the predicted Dirichlet distribution $\text{Dir}(\boldsymbol{\alpha})$, parameterized by the ENN. In practice, this ground truth is typically inaccessible.

Aleatoric uncertainty (uncertainty of the class prediction) can be calculated with the negative maximum class probability or the entropy of the categorical distribution. Ideally, aleatoric uncertainty should reflect the model's confidence in a perfectly calibrated network. However, over-parameterized deep neural networks, trained with the conventional cross-entropy objective, often exhibit overconfidence, leading to significant calibration issues (Guo et al., 2017). The overconfidence issue is frequently correlated with overfitting the negative log-likelihood (NLL), since even with a classification error of zero (indicative of perfect calibration), the NLL can remain positive. The optimization algorithm may continue to reduce this value by increasing the probability of the predicted class. In this section, we demonstrate that the UCE loss suffers from a similar issue. For example, even with perfect evidence volume prediction, the UCE loss remains positive and increasing the evidence for the predicted class further decreases the UCE loss. To address this, we propose the UFCE loss, which aims to improve both model calibration and segmentation performance.

Epistemic uncertainty (uncertainty on the categorical distribution) can be calculated with the predicted total evidence α_0. In the commonly used UCE loss (Sensoy et al., 2018; Charpentier et al., 2020), minimization continues when total evidence increases. Bengs et al. (2022) highlighted that learners employing UCE loss with first-level ground truth (class label) tend to peak the third-level distribution (Dirichlet distribution). This creates a false impression of complete certainty rather than accurately reflecting uncertainty. To address this, we propose epistemic uncertainty scaling and regularized evidential learning to improve epistemic uncertainty prediction.

Overall, aleatoric and epistemic uncertainty can be estimated based on the Dirichlet parameters $\boldsymbol{\alpha}$:

$$u^{alea} = -\max_c \bar{p}_c, \; u^{epis} = C/\alpha_0, \tag{6}$$

Proposition 1. *Given a predicted distribution $\boldsymbol{p} \sim \texttt{Dir}(\boldsymbol{\alpha})$, where $\boldsymbol{\alpha} = (\alpha_1, \alpha_2, \ldots, \alpha_C)$ and C is the number of categories, and a target distribution $\boldsymbol{q} \sim \texttt{Dir}(\hat{\boldsymbol{\alpha}})$, assuming a one-hot style target distribution such that $\hat{\alpha}_i = 1$ for all $i \neq c^*$ where c^* is the ground truth label and $\hat{\alpha}_{c^*} = 2$, we have the following loss function:*

$$\mathcal{L}^{UCE} = KL(\texttt{Dir}(\boldsymbol{\alpha}) \parallel \texttt{Dir}(\hat{\boldsymbol{\alpha}})) + H(\texttt{Dir}(\boldsymbol{\alpha})) - \log(B(\hat{\boldsymbol{\alpha}})) \tag{7}$$

where $\log(B(\hat{\boldsymbol{\alpha}}))$ is a constant. Proposition 1 reveals that the optimization of UCE loss is minimizing the summation over the Kullback-Leibler (KL) divergence between the predicted and ground truth distributions and the entropy of the predicted distribution. Therefore, minimizing UCE loss will push the predicted Dirichlet distribution close to the one-hot target evidence distribution, and peak it simultaneously, resulting in a peaked distribution profile that is over-confident.

3.2 UFCE - IMPLICIT WEIGHT REGULARIZATION

Motivated by the better calibration capability of Focal loss (Lin et al., 2017) compared to cross-entropy, we propose the Uncertainty Focal Cross Entropy (UFCE) loss, which takes the expectation of focal loss rather than cross-entropy loss.

$$\begin{aligned}\mathcal{L}^{\text{UFCE}}(\boldsymbol{\theta}, \boldsymbol{X}, \boldsymbol{y}) &= \mathbb{E}_{(\boldsymbol{X},\boldsymbol{y})\sim\mathcal{D}^{train}}\mathbb{E}_{\mathbf{p}\sim\text{Dir}(\boldsymbol{\alpha}(\boldsymbol{\theta},\boldsymbol{X}))}\left[-\sum_{c=1}^{C} y_c(1-p_c)^{\gamma}\log p_c\right] \\ &= \mathbb{E}_{(\boldsymbol{X},\boldsymbol{y})\sim\mathcal{D}^{train}}\left(\frac{B(\alpha_0,\gamma)}{B(\alpha_0-\alpha_{c^*},\gamma)}\left[\psi(\alpha_0+\gamma)-\psi(\alpha_{c^*})\right]\right)\end{aligned} \tag{8}$$

where γ is a hyperparameter, c^* is the ground truth class index, and $B(\cdot)$ is the Beta function. When $\gamma = 0$, the UFCE loss is equivalent to the UCE loss.

Why does UFCE loss improve calibration over UCE loss? The general form of the UFCE loss has a lower bound involving the UCE loss as follows (see Appendix Proposition 4):

$$\mathcal{L}^{\text{UFCE}} \geq \mathcal{L}^{\text{UCE}} - \gamma \cdot \mathbb{E}_{\mathbf{p}\sim\text{Dir}(\boldsymbol{\alpha})}\big[H(\mathbf{p})\big] \tag{9}$$

where the second term in the lower bound is the expectation of the entropy function ($H(\mathbf{p})$) of the categorical distribution $\text{Cat}(\mathbf{p})$ based on $\text{Dir}(\boldsymbol{\alpha})$. This bound indicates that minimizing UFCE loss results in minimizing the weighted difference between the UCE loss and the second term, where γ plays the role of a trade-off between these two terms. Maximizing the second term tends to push down α_{c^*} to be close to the evidence of false classes α_c, $\forall c \neq c^*$, implying that the UFCE loss models are relatively less confident in evidence predictions than the UCE loss models for samples that they classify correctly.

In the proposition below, we consider the influence of gradients on the prediction of α_{c^*}. Let $\mathbf{w}_{c^*}$ denote the weight parameters in the last linear layer that influence the prediction of α_{c^*}.

Proposition 2. *Comparing $\mathcal{L}^{UFCE}$ and $\mathcal{L}^{UCE}$ with numerical analysis on the gradient of the parameters $\mathbf{w}_{c^*}$ in the last linear layer, we have,*

$$\left\|\frac{\partial\mathcal{L}^{UFCE}}{\partial\mathbf{w}_{c^*}}\right\| - \left\|\frac{\partial\mathcal{L}^{UCE}}{\partial\mathbf{w}_{c^*}}\right\| \begin{cases}\geq 0 & \text{if } \bar{p}_{c^*} \leq \tau_1(\alpha_{c^*},\gamma) \\ < 0 & \text{if } \bar{p}_{c^*} > \tau_2(\alpha_{c^*},\gamma)\end{cases},$$

where $\tau_1(\alpha_{c^*},\gamma)$ and $\tau_2(\alpha_{c^*},\gamma)$ are two thresholds within $(\frac{1}{\alpha_0}, 1-\frac{1}{\alpha_0})$. respectively.

Proposition 2 shows the relationship between the norms of the gradients of the last linear layer for UFCE and UCE loss under the same network architecture. It is clear that for every γ and α_{c^*}, there exists a threshold τ_1 such that for all $\bar{p}_{c^*} \in (\frac{1}{\alpha_0}, \tau_1]$, $\left\|\frac{\partial\mathcal{L}^{\text{UFCE}}}{\partial\mathbf{w}_{c^*}}\right\| \geq \left\|\frac{\partial\mathcal{L}^{\text{UCE}}}{\partial\mathbf{w}_{c^*}}\right\|$. This implies that the evidence belonging to the ground truth class predicted by the UFCE mode will initially increase faster than that of the UCE model.

Moreover, there exists a τ_2, and for all $\bar{p}_{c^*} \in [\tau_2, 1-\frac{1}{\alpha_0})$, $\left\|\frac{\partial\mathcal{L}^{\text{UFCE}}}{\partial\mathbf{w}_{c^*}}\right\| \leq \left\|\frac{\partial\mathcal{L}^{\text{UCE}}}{\partial\mathbf{w}_{c^*}}\right\|$. It implies once p_{c^*} surpasses the threshold τ, UFCE will apply a regularizing effect to prevent the model from continuing to focus on examples it is already confident about, thus avoiding overfitting.

Figure 1 shows an example with $\gamma = 1$ and $\alpha_{c^*} = 5$, $\tau_1 = \tau_2 \approx 0.4$. This also implicitly acts as a weight regularizer by pushing the model to focus more on less confident scenarios, which is crucial for highly imbalanced data. Further analysis can be found in Figure 2 and Figure 3.

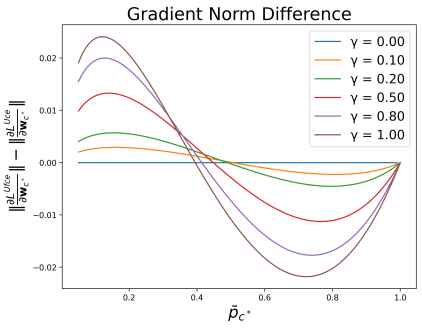

Figure 1: The y-axis is the difference between the l1-norm of the UFCE gradient and the norm of the UCE gradient with fixed $\alpha_{c^*} = 5$. The x-axis is the $\bar{p}_{c^*}$ which is the expected predicted class probability belonging to the ground truth class.

3.3 UNCERTAINTY QUANTIFICATION FRAMEWORK

Epistemic uncertainty scaling (EUS): Owing to the imbalance between in-distribution (ID) and OOD pixels within the BEVSS datasets, we observe a tendency for the model to erroneously classify ID pixels that are proximal to OOD objects. This often leads to the model assigning low confidence to these ID pixels, resulting in high epistemic uncertainty. Consequently, this issue significantly increases the occurrence of false positives during the OOD detection task. To address this, we propose using epistemic uncertainty scaling to explicitly apply different weights for samples based on their predicted epistemic uncertainty in the previous step of optimization. The equation 8 is adjusted to:

$$\mathcal{L}^{\text{UFCE-EUS}} = \left(1 + \frac{C \cdot \xi}{\alpha_0}\right) \cdot \mathcal{L}^{\text{UFCE}} \tag{10}$$

where ξ is a hyperparameter and α_0 is the value predicted by the neural network in the previous optimization step. An example with low evidence in the training set will catch more attention during the training process and may lead to better performance on such "difficult" samples.

Evidence-Regularized Learning (ER). We consider the OOD-exposure setting to further enhance the epistemic uncertainty estimation. Assume $\mathcal{D}_{in}^{train}$ is the ID training data and $\mathcal{D}_{out}^{train}$ is the auxiliary OOD training data. Note that we have true OOD ($\mathcal{D}_{out}^{test}$) for the evaluation where the auxiliary OOD and true OOD belong to different distributions. We propose training the model to minimize the KL divergence between predictions and a flat Dirichlet distribution for these auxiliary OOD samples.

$$\mathcal{L}^{\text{ER}} = \mathbb{E}_{(\boldsymbol{X}_{out}, \boldsymbol{y}) \sim \mathcal{D}_{out}^{train}} \text{KL}\left(\text{Dir}(\boldsymbol{\alpha}) \parallel \text{Dir}(\mathbf{1})\right) \tag{11}$$

For fair comparison, we also include a setting with OOD exposure for the energy-based model. With the same strategy as (Liu et al., 2020), we consider energy-bounded learning for OOD detection. Details can be found in Appendix A.2.3.

Proposed framework: We replace the last softmax activation function of the original BEVSS model with a ReLU function in order to produce concentrated parameters for pixel-wise Dirichlet distribution. The model is optimized by the following objective functions:

$$\mathcal{L}^{\text{UFCE-EUS-ER}} = \mathcal{L}^{\text{UFCE-EUS}} + \lambda \mathcal{L}^{\text{ER}} \tag{12}$$

Our proposed framework comprises three primary components: the Uncertainty Focal Cross-Entropy (UFCE) loss, Evidential Regularizer (ER), and epistemic uncertainty scaling (EUS). We consider three hyperparameters. γ in the UFCE, ξ in the VS and λ for the ER term.

4 EXPERIMENTS

In this section, we introduce a benchmark that evaluates uncertainty-aware BEVSS. This benchmark includes three datasets, two BEVSS backbones, five uncertainty quantification models, and two uncertainty estimation tasks. We address the following research questions:

RQ1: Are aleatoric and epistemic uncertainties estimated by these models reliable? Specifically, can the aleatoric uncertainty metrics accurately detect misclassified pixels, and can the epistemic uncertainty metrics effectively identify OOD samples?

RQ2: Does our proposed UFCE loss enhance model performance in terms of calibration in comparison to the traditionally utilized UCE loss in ENNs?

RQ3: Does the proposed uncertainty quantification framework improve the prediction of epistemic uncertainty as evaluated by the OOD detection task?

Following these three research questions, we provided extensive experiments and further discussions.

4.1 BENCHMARK SETUPS

Evaluation. Following the task setting from (Philion & Fidler, 2020) and (Zhou & Krähenbühl, 2022), we conduct both vehicle segmentation and drivable area segmentation. We evaluate performance using four metrics: (1) *Pure segmentation* via Intersection-over-Union (IoU). (2) *Calibration* via

Expected Calibration Error (ECE). (3) *Aleatoric Uncertainty* via the misclassification detection to identify the misclassified pixels, measured with Area Under ROC Curve (AUROC) and Area Under PR Curve (AUPR). (4) *Epistemic Uncertainty* via the OOD detection to identify the OOD pixels, measured with AUROC and AUPR.

Datasets. We utilize a dataset generated with the CARLA simulator, three real-world datasets (nuScenes and Lyft), and a corrupted dataset, nuScenes-C (Xie et al., 2024). In the default setting, "motorcycle" and "bicycle" are used as the true OOD and pseudo-OOD for nuScenes and Lyft, respectively, while "deer" serves as the true OOD, and "bears, horses, cows, elephants" as pseudo-OODs for CARLA. To evaluate robustness to pseudo-OOD choices, an alternative configuration uses "traffic cones, pushable/pullable objects, motorcycles" as pseudo-OOD and "barriers" as true OOD for nuScenes, and "kangaroo" as true OOD for CARLA, which has lower similarity to the pseudo-OOD comparing to default setting. Detailed dataset descriptions and statistics are in Appendix A.4.

BEVSS Backbones. We utilize LSS, CVT, and Simple-BEV as model backbones with publicly available implementations. LSS converts raw camera inputs into BEV representations by predicting depth distributions, constructing feature frustums, and rasterizing them onto a BEV grid, while CVT employs a transformer-based approach with cross-attention and camera-aware positional embeddings to align features into the BEV space. In contrast, Simple-BEV bypasses depth estimation entirely, projecting 3D coordinate volumes onto camera images to sample features, emphasizing efficiency and robustness to projection errors. Detailed descriptions can be found in Appendix A.2.1.

Uncertainty quantification baselines. We consider widely used uncertainty quantification models in traditional deep learning. The "Entropy" and "Energy" models perform post-hoc processing on predicted logits, with the "Energy" model being particularly popular for its adaptability and strong OOD detection performance. We also include the "Dropout" and "Ensemble" models, which are commonly applied in various domains with Bayesian interpretations. The "Ensemble" model uses three separately trained models initialized with different random seeds, while the "Dropout" model employs activated dropout layers during inference, performing 10 forward passes. Both models utilize either cross-entropy or focal loss. Lastly, we use the "ENN" model with UCE loss as a baseline. Notably, both "Energy" and "ENN" models can be trained with or without pseudo-OOD information. Details can be found in Appendix A.2.3.

Hyperparameters. LSS and CVT are trained with a batch size of 32, while Simple-BEV uses a batch size of 16, all for 20 epochs on NVIDIA A6000 or A100 GPUs. Backbone-specific hyperparameters for LSS, CVT, and Simple-BEV are adopted from their original studies. We use the learning rate scheduler from CVT, setting the learning rate to 4e-3 for focal loss variants (as in CVT) and 1e-3 for cross-entropy variants (as in LSS), with the Adam optimizer and a weight decay of 1e-7, consistent with both LSS and CVT.

We tune three regularization weights, λ, ξ, and γ, based on the AUPR metric for pseudo-OOD detection on the validation set. To manage computational complexity, we adopt a step-by-step tuning approach, fixing two parameters while adjusting the third, instead of performing a full grid search. Detailed information on hyperparameter tuning strategy, optimal values, and sensitivity analysis can be found in Appendix A.3.1.

4.2 Results

In the main paper, we present results on nuScenes using LSS and CVT as backbones, covering predicted segmentation and aleatoric uncertainty (Table 1), epistemic uncertainty (Table 2), running time (Table 3), robustness analysis (Table 4), and ablation studies (Table 5).

In the appendix, we provide results on CARLA and Lyft using all backbones including LSS, CVT, and Simple-BEV (Tables 13–16). Additionally, we include hyperparameter analysis (Tables 7–9) and robustness experiments (Tables 17–23), which encompass detailed results on corrupted nuScenes-C, diverse town and weather conditions in CARLA, and pseudo-OOD selections. Qualitative comparisons are provided in Figures 4–6.

Benchmark Observations (RQ1): Pure segmentation: (1) Across a comprehensive range of configurations (50 in total), focal-based losses demonstrate superior segmentation performance when compared to the standard cross-entropy loss in all but two instances, where the difference is marginal (within 0.7%). This pattern is particularly pronounced in models utilizing the CVT backbone, where

Table 1: Calibration and misclassification detection performance on the nuScence dataset for vehicle segmentation. Best and Runner-up results are highlighted in red and blue.

Model	Loss	LSS					CVT				
		Pure Classification		Misclassification			Pure Classification		Misclassification		
		IoU ↑	ECE↓	AUROC ↑	AUPR ↑	FPR95 ↓	IoU ↑	ECE↓	AUROC ↑	AUPR ↑	FPR95 ↓
Without pseudo OOD											
Entropy	CE	0.332	0.00887	0.909	0.315	0.234	0.277	0.00374	0.949	0.325	0.213
	Focal	0.347	0.00301	0.941	0.332	0.197	0.325	0.00341	0.949	0.321	0.206
Energy	CE	0.332	0.00887	0.909	0.315	0.234	0.277	0.00374	0.949	0.325	0.213
	Focal	0.347	0.00301	0.941	0.332	0.197	0.325	0.00341	0.949	0.321	0.206
Ensemble	CE	0.355	0.00569	0.933	0.317	0.218	0.301	0.00276	0.951	0.315	0.216
	Focal	0.37	0.00233	0.946	0.315	0.203	0.344	0.00243	0.953	0.324	0.195
Dropout	CE	0.332	0.00819	0.905	0.315	0.235	0.279	0.00373	0.946	0.332	0.213
	Focal	0.347	0.00261	0.936	0.325	0.208	0.325	0.00363	0.948	0.327	0.202
ENN	UCE	0.341	0.00429	0.819	0.273	0.335	0.291	0.00371	0.900	0.305	0.224
	UFCE	0.343	0.00332	0.873	0.310	0.225	0.319	0.0019	0.918	0.319	0.208
With pseudo OOD											
Energy	CE	0.348	0.00721	0.949	0.331	0.200	0.296	0.00238	0.951	0.316	0.219
	Focal	0.346	0.00466	0.951	0.331	0.192	0.333	0.00186	0.955	0.321	0.196
ENN	UCE	0.343	0.00342	0.838	0.288	0.296	0.282	0.00336	0.919	0.313	0.227
	Ours	0.356	0.00193	0.911	0.317	0.190	0.319	0.00019	0.934	0.321	0.196

Observations: 1. Involving pseudo-OOD in the training phase does not impact pure segmentation, calibration and misclassification detection. 2. Without pseudo-OOD, the proposed UFCE loss for the ENN model consistently outperforms the commonly used UCE loss across all metrics, showing average improvements of 0.0014 in calibration ECE, 3.6% in misclassification AUROC, 2.5% in AUPR and 6.3% on FPR95 across two backbones. 3. No single model consistently performs best across all metrics, but Focal consistently performs better than CE.

Table 2: OOD detection performance for vehicle segmentation . Best and Runner-up results are highlighted in red and blue.

Model	Loss	nuScenes						CARLA					
		LSS			CVT			LSS			CVT		
		AUROC ↑	AUPR ↑	FPR95 ↓	AUROC ↑	AUPR ↑	FPR95 ↓	AUROC ↑	AUPR ↑	FPR95 ↓	AUROC ↑	AUPR ↑	FPR95↓
Without pseudo OOD													
Entropy	CE	0.584	0.000523	0.799	0.728	0.000568	0.824	0.693	0.00236	0.782	0.813	0.00307	0.704
	Focal	0.647	0.000562	0.764	0.69	0.000527	0.828	0.693	0.00236	0.782	0.794	0.00271	0.736
Energy	CE	0.602	0.000494	0.794	0.72	0.000596	0.801	0.683	0.00217	0.762	0.813	0.00304	0.708
	Focal	0.564	0.000496	0.781	0.639	0.000534	0.823	0.683	0.00217	0.762	0.788	0.00265	0.737
Ensemble	CE	0.385	0.000159	0.979	0.478	0.000205	0.96	0.488	0.000655	0.965	0.505	0.000679	0.963
	Focal	0.537	0.000245	0.941	0.503	0.000212	0.964	0.455	0.000655	0.953	0.491	0.000668	0.962
Dropout	CE	0.411	0.000174	0.975	0.384	0.000171	0.957	0.441	0.000616	0.966	0.36	0.000522	0.971
	Focal	0.348	0.00015	0.994	0.402	0.000192	0.931	0.39	0.00056	0.964	0.317	0.000487	0.974
ENN	UCE	0.717	0.000748	0.791	0.661	0.000488	0.857	0.62	0.00172	0.795	0.685	0.00235	0.814
	UFCE	0.518	0.000338	0.892	0.683	0.00066	0.816	0.535	0.00163	0.835	0.748	0.00237	0.775
With pseudo OOD													
Energy	CE	0.774	0.0474	0.408	0.839	0.0206	0.356	0.897	0.0745	0.259	0.929	0.0514	0.159
	Focal	0.821	0.0444	0.378	0.86	0.0237	0.319	0.908	0.078	0.183	0.948	0.0788	0.137
ENN	UCE	0.889	0.315	0.315	0.921	0.212	0.306	0.889	0.147	0.272	0.97	0.111	0.161
	Ours	0.929	0.335	0.219	0.928	0.269	0.244	0.96	0.204	0.18	0.979	0.237	0.125

Observations: 1. Without pseudo-OOD, no uncertainty quantification models can predict satisfying epistemic uncertainty, as shown by extremely low OOD detection PR, implying epistemic uncertainty estimation is challenging for BEVSS. 2. Compared to all baselines, our proposed model (last line in the table) has the best OOD detection performance on all 12 metrics, with an average improvement of 2.7% in AUROC, 6.5% in AUPR and 4.3% in FPR95 over the runner-up model.

focal-based losses yield more significant improvements. (2) The UFCE loss for the ENN consistently outperforms the UCE loss across all 14 configurations. Calibration: In the majority of scenarios, models with focal-based loss exhibit lower ECE scores, indicating better calibration than cross-entropy based models. Similarly, UFCE consistently outperforms UCE. No single model consistently performs best in terms of calibration. Misclassification detection: (1) Despite most models achieving AUROC scores over 90%, the AUPR values remain below 40% across two datasets, indicating significant room for improvement in aleatoric uncertainty estimation. (2) Models using a focal-based loss perform better in misclassification detection across most settings compared to those using a CE-based loss.

Table 3: Running time

Model	Task	Energy	Ensemble	Dropout	ENN-UCE	ENN-UFCE	Ours
LSS	Training	10 hours	30 hours	10 hours	10 hours	10 hours	10 hours
	Inference	54 ms	147 ms	457 ms	55 ms	51 ms	56 ms
CVT	Training	8 hours	24 hours	8 hours	8 hours	8 hours	8 hours
	Inference	15 ms	32 ms	123 ms	14 ms	16 ms	15 ms

OOD detection: (1) Without pseudo-OOD exposure, all models perform poorly in OOD detection, as evidenced by low AUPR values. (2) Only the energy-based and evidential-based models can utilize pseudo-OOD data. With pseudo-OOD exposure, both models show significant improvements in AUROC and AUPR, indicating that utilizing pseudo-OODs may be a promising direction. Our proposed framework achieves the highest OOD detection performance across all eight evaluated settings. (3) OOD detection in BEVSS is a challenging task, as evidenced by the low AUPR.

Complexity analysis: Table 3 presents the estimated duration for training on a pair of A100 GPUs and inference on a single A6000 GPU. Ensemble models require significantly more time for training, whereas the Dropout model incurs a longer duration during inference. Conversely, the ENN demonstrates reduced time complexity for both training and inference processes. Our proposed model has similar training and inference time cost with the energy model.

Analysis of UFCE Loss (RQ2): We discuss the effect of UFCE loss from three views. Calibration: (1) Compared to UCE loss without pseudo-OOD exposure, models using UFCE loss achieve higher IoU and lower ECE scores across most configurations for vehicle detection and driveable region detection tasks on three datasets and two backbone architectures. Additionally, under pseudo-OOD supervision, UFCE-based models consistently show better IoU and ECE scores across all experimental setups, highlighting UFCE's superior segmentation accuracy and model calibration. (2) Compared to all models with the same configuration, the ENN using UFCE loss achieves results comparable to those designed solely for segmentation. Notably, the ENN with UFCE loss achieves the lowest ECE score on 4 out of 6 configurations and another second lowest one 1 configuration, demonstrating its effectiveness in calibration. Misclassification detection: UFCE loss outperforms UCE loss with consistently higher AUROC and AUPR scores. Among all models, UFCE's performance generally ranks in the middle to upper echelon. Notably, with pseudo-OOD exposure, the ENN shows improved segmentation performance. This enhancement is due to the model's better capability to predict more accurate Dirichlet distributions, especially for pixels near OOD instances.

Table 4: Robustness study on the selection of pseudo-OOD with vehicle segmentation task on nuScenes. Best and Runner-up results are highlighted in red and blue.

Model	LSS			CVT		
	OOD Detection			OOD Detection		
	AUROC ↑	AUPR ↑	FPR95 ↓	AUROC ↑	AUPR ↑	FPR95 ↓
UFCE-EUS-ER	0.895	0.215	0.274	0.94	0.153	0.272
UCE-EUS-ER	0.914	0.208	0.291	0.908	0.117	0.346
UCE-ER	0.862	0.192	0.302	0.887	0.0934	0.354
UFCE	0.495	0.000609	0.919	0.727	0.00118	0.861

We evaluate the alternative pseudo-OOD setting, using traffic cones, pushable/pullable objects, and motorcycles as pseudo-OOD, with barriers as the true OOD. Our model outperforms the runner-up in 5 out of 6 metrics, achieving an average AUPR improvement of 18%, with both UFCE and EUS significantly contributing to these gains.

OOD detection: Compared to UCE loss with pseudo-OOD supervision, our proposed framework with UFCE loss demonstrates significantly better performance, with up to a 12% increase in AUPR and a 4% boost in AUROC. These results highlight the significant potential of the UFCE approach to improve the reliability of epistemic uncertainty estimation.

Table 5: Ablation study for vehicle segmentation on nuScenes . Best and Runner-up results are highlighted in red and blue.

Model	Pure Classification		Misclassification			OOD Detection		
	IoU ↑	ECE ↓	AUROC ↑	AUPR ↑	FPR95 ↓	AUROC ↑	AUPR ↑	FPR95 ↓
LSS								
UFCE-EUS-ER	0.356	0.00193	0.911	0.317	0.19	0.929	0.335	0.219
UCE-EUS-ER	0.339	0.00363	0.842	0.29	0.29	0.842	0.34	0.329
UCE-ER	0.342	0.00342	0.838	0.289	0.296	0.889	0.315	0.315
UCE	0.341	0.00429	0.819	0.273	0.335	0.717	0.000748	0.791
CVT								
UFCE-EUS-ER	0.319	0.00019	0.934	0.321	0.196	0.928	0.269	0.244
UCE-EUS-ER	0.281	0.0036	0.92	0.314	0.217	0.931	0.21	0.326
UCE-ER	0.282	0.00336	0.919	0.313	0.227	0.921	0.212	0.306
UCE	0.291	0.00371	0.9	0.305	0.224	0.661	0.000488	0.857

The base model is "UCE" and we progressively add the proposed components. First, we introduce ER to obtain "UCE-ER", followed by adding EUS to create "UCE-EUS-ER". Finally, we replace UCE with UFCE, resulting in the model "UFCE-EUS-ER". **Observation:** Adding "ER" largely improve the OOD detection performance (average 26%), "EUS" further improve he misclassification detection and OOD detection slightly. The "UFCE" improves the calibration and misclassification detection with a significant gap (ECE:0.002555, AUROC:4.15%, AUPR:1.7%, FPR95:6.05%)

Ablation Study (RQ3): There are three primary components: UFCE, EUS, ER. We conduct ablation studies using the nuScenes dataset with LSS and CVT backbones to assess the impact of each component on system performance without compromising generality. The results are summarized in Table 5. Starting with the standard ENN model using the UCE loss as the baseline, we progressively add components to assess their contributions. First, we introduce the ER term, which incorporates pseudo-OOD data during training. This addition leads to a significant improvement in OOD detection performance, with up to a 31% improvement in AUPR. Next, we add the EUS regularization, which further enhances both misclassification detection and OOD detection performance. Finally, we replace the UCE loss with our proposed UFCE loss, achieving the best overall results. This change results in up to a 6% improvement in AUPR, particularly benefiting calibration and misclassification detection without sacrificing segmentation accuracy.

Discussion on the pseudo-OOD: Intuitively, greater similarity between true and pseudo-OOD pairs enhances OOD detection performance, while overfitting to pseudo-OODs raises concerns about the model's generalization ability. To further investigate, we conducted experiments using dissimilar pseudo-OOD and true OOD pairs compared to the default setting (Table 2). The results for nuScenes are shown in Table 4, while the results for CARLA are provided in Table 17 in Appendix A.5.5. The findings confirm our intuition: higher similarity between true and pseudo-OOD pairs leads to better OOD detection performance. Notably, our proposed model consistently outperformed the best baseline methods across all eight scenarios, achieving improvements of up to 12.6% in AUPR. These results underscore the robustness of our approach, even in settings with less similar OOD pairs.

5 Conclusion

This paper presents a comprehensive evaluation of various uncertainty quantification methods for BEVSS. Our findings reveal that current methods do not achieve satisfactory results in uncertainty quantification, particularly in OOD detection, highlighting the need for advancements in this domain. Inspired by the robust calibration properties of Focal Loss, we introduce the UFCE loss, which significantly enhances model calibration. Our proposed uncertainty quantification framework, based on evidential deep learning, consistently outperforms baseline models in predicting epistemic uncertainty, as well as in aleatoric uncertainty and calibration, across a wide range of scenarios.

REFERENCES

Siddharth Ancha, Philip R Osteen, and Nicholas Roy. Deep evidential uncertainty estimation for semantic segmentation under out-of-distribution obstacles. In *Proc. IEEE Int. Conf. Robot. Autom*, 2024.

J. Behley, M. Garbade, A. Milioto, J. Quenzel, S. Behnke, C. Stachniss, and J. Gall. SemanticKITTI: A Dataset for Semantic Scene Understanding of LiDAR Sequences. In *Proc. of the IEEE/CVF International Conf. on Computer Vision (ICCV)*, 2019.

Viktor Bengs, Eyke Hüllermeier, and Willem Waegeman. Pitfalls of epistemic uncertainty quantification through loss minimisation. *Advances in Neural Information Processing Systems*, 35: 29205–29216, 2022.

Holger Caesar, Varun Bankiti, Alex H. Lang, Sourabh Vora, Venice Erin Liong, Qiang Xu, Anush Krishnan, Yu Pan, Giancarlo Baldan, and Oscar Beijbom. nuscenes: A multimodal dataset for autonomous driving. In *CVPR*, 2020.

Loick Chambon, Eloi Zablocki, Mickaël Chen, Florent Bartoccioni, Patrick Pérez, and Matthieu Cord. Pointbev: A sparse approach for bev predictions. In *Proceedings of the IEEE/CVF Conference on Computer Vision and Pattern Recognition*, pp. 15195–15204, 2024.

Bertrand Charpentier, Daniel Zügner, and Stephan Günnemann. Posterior network: Uncertainty estimation without ood samples via density-based pseudo-counts. *Advances in Neural Information Processing Systems*, 33:1356–1367, 2020.

Vikrant Dewangan, Basant Sharma, Tushar Choudhary, Sarthak Sharma, Aakash Aanegola, Arun K Singh, and K Madhava Krishna. Uap-bev: Uncertainty aware planning using bird's eye view generated from surround monocular images. In *2023 IEEE 19th International Conference on Automation Science and Engineering (CASE)*, pp. 1–8. IEEE, 2023.

Alexey Dosovitskiy, German Ros, Felipe Codevilla, Antonio Lopez, and Vladlen Koltun. CARLA: An open urban driving simulator. In *Proceedings of the 1st Annual Conference on Robot Learning*, pp. 1–16, 2017.

Florian Fervers, Sebastian Bullinger, Christoph Bodensteiner, Michael Arens, and Rainer Stiefelhagen. Uncertainty-aware vision-based metric cross-view geolocalization. In *Proceedings of the IEEE/CVF Conference on Computer Vision and Pattern Recognition*, pp. 21621–21631, 2023.

Gianni Franchi, Xuanlong Yu, Andrei Bursuc, Angel Tena, Rémi Kazmierczak, Séverine Dubuisson, Emanuel Aldea, and David Filliat. Muad: Multiple uncertainties for autonomous driving, a benchmark for multiple uncertainty types and tasks. *arXiv preprint arXiv:2203.01437*, 2022.

Yarin Gal and Zoubin Ghahramani. Dropout as a bayesian approximation: Representing model uncertainty in deep learning. In Maria-Florina Balcan and Kilian Q. Weinberger (eds.), *Proceedings of the 33nd International Conference on Machine Learning, ICML 2016, New York City, NY, USA, June 19-24, 2016*, volume 48 of *JMLR Workshop and Conference Proceedings*, pp. 1050–1059. JMLR.org, 2016. URL `http://proceedings.mlr.press/v48/gal16.html`.

Joshua Goodman. The uber self-driving car fatality: what happened, and what it means. *IEEE Spectrum*, 28, 2018. URL `https://en.wikipedia.org/wiki/Death_of_Elaine_Herzberg`.

Chuan Guo, Geoff Pleiss, Yu Sun, and Kilian Q Weinberger. On calibration of modern neural networks. In *ICML*, pp. 1321–1330. PMLR, 2017.

Adam W Harley, Zhaoyuan Fang, Jie Li, Rares Ambrus, and Katerina Fragkiadaki. Simple-bev: What really matters for multi-sensor bev perception? In *2023 IEEE International Conference on Robotics and Automation (ICRA)*, pp. 2759–2765. IEEE, 2023.

Dan Hendrycks and Kevin Gimpel. A baseline for detecting misclassified and out-of-distribution examples in neural networks. *arXiv preprint arXiv:1610.02136*, 2016.

Anthony Hu, Zak Murez, Nikhil Mohan, Sofía Dudas, Jeffrey Hawke, Vijay Badrinarayanan, Roberto Cipolla, and Alex Kendall. Fiery: future instance prediction in bird's-eye view from surround monocular cameras. In *Proceedings of the IEEE/CVF International Conference on Computer Vision*, pp. 15273–15282, 2021.

Junjie Huang, Guan Huang, Zheng Zhu, and Dalong Du. Bevdet: High-performance multi-camera 3d object detection in bird-eye-view. *ArXiv*, abs/2112.11790, 2021.

Audun Jøsang. *Subjective logic*, volume 3. Springer, 2016.

Markus Kängsepp and Meelis Kull. Calibrated perception uncertainty across objects and regions in bird's-eye-view. *arXiv preprint arXiv:2211.04340*, 2022.

Alex Kendall and Yarin Gal. What uncertainties do we need in bayesian deep learning for computer vision? *Advances in neural information processing systems*, 30, 2017.

R. Kesten, M. Usman, J. Houston, T. Pandya, K. Nadhamuni, A. Ferreira, M. Yuan, B. Low, A. Jain, P. Ondruska, S. Omari, S. Shah, A. Kulkarni, A. Kazakova, C. Tao, L. Platinsky, W. Jiang, and V. Shet. Lyft level 5 av dataset 2019. `https://level5.lyft.com/dataset/`, 2019.

Balaji Lakshminarayanan, Alexander Pritzel, and Charles Blundell. Simple and scalable predictive uncertainty estimation using deep ensembles. *NeurIPS*, 30, 2017.

Alex H. Lang, Sourabh Vora, Holger Caesar, Lubing Zhou, Jiong Yang, and Oscar Beijbom. Pointpillars: Fast encoders for object detection from point clouds. *2019 IEEE/CVF Conference on Computer Vision and Pattern Recognition (CVPR)*, pp. 12689–12697, 2018.

Tsung-Yi Lin, Priya Goyal, Ross Girshick, Kaiming He, and Piotr Dollár. Focal loss for dense object detection. In *Proceedings of the IEEE international conference on computer vision*, pp. 2980–2988, 2017.

Weitang Liu, Xiaoyun Wang, John Owens, and Yixuan Li. Energy-based out-of-distribution detection. *Advances in neural information processing systems*, 33:21464–21475, 2020.

Zhijian Liu, Haotian Tang, Alexander Amini, Xinyu Yang, Huizi Mao, Daniela L Rus, and Song Han. Bevfusion: Multi-task multi-sensor fusion with unified bird's-eye view representation. In *2023 IEEE international conference on robotics and automation (ICRA)*, pp. 2774–2781. IEEE, 2023.

Jishnu Mukhoti and Yarin Gal. Evaluating bayesian deep learning methods for semantic segmentation. *arXiv preprint arXiv:1811.12709*, 2018.

Jishnu Mukhoti, Joost van Amersfoort, Philip HS Torr, and Yarin Gal. Deep deterministic uncertainty for semantic segmentation. *arXiv preprint arXiv:2111.00079*, 2021.

Jonah Philion and Sanja Fidler. Lift, splat, shoot: Encoding images from arbitrary camera rigs by implicitly unprojecting to 3d. In *ECCV*, 2020.

Murat Sensoy, Lance Kaplan, and Melih Kandemir. Evidential deep learning to quantify classification uncertainty. *NeurIPS*, 31, 2018.

David Shepardson. Tesla autopilot involved in crash with parked police car in florida. *Reuters*, 2022. URL `https://www.cnn.com/2021/08/30/business/tesla-crash-police-car/index.html`.

Mingxing Tan and Quoc V. Le. Efficientnet: Rethinking model scaling for convolutional neural networks. *ArXiv*, abs/1905.11946, 2019.

Xiao Wang, Hongrui Liu, Chuan Shi, and Cheng Yang. Be confident! towards trustworthy graph neural networks via confidence calibration. *Advances in Neural Information Processing Systems*, 34:23768–23779, 2021.

Shaoyuan Xie, Lingdong Kong, Wenwei Zhang, Jiawei Ren, Liang Pan, Kai Chen, and Ziwei Liu. Benchmarking and improving bird's eye view perception robustness in autonomous driving. *arXiv preprint arXiv:2405.17426*, 2024.

Brady Zhou and Philipp Krähenbühl. Cross-view transformers for real-time map-view semantic segmentation. In *Proceedings of the IEEE/CVF Conference on Computer Vision and Pattern Recognition*, pp. 13760–13769, 2022.

Xiyue Zhu, Vlas Zyrianov, Zhijian Liu, and Shenlong Wang. Mapprior: Bird's-eye view map layout estimation with generative models. In *Proceedings of the IEEE/CVF International Conference on Computer Vision*, pp. 8228–8239, 2023.

A APPENDIX

A.1 PROOFS

Assume the target distribution $\boldsymbol{q} \sim \text{Dir}(\hat{\boldsymbol{\alpha}})$ and the predicted distribution $\boldsymbol{p} \sim \text{Dir}(\boldsymbol{\alpha})$, where $\boldsymbol{\alpha} = (\alpha_1, \alpha_2, \ldots, \alpha_C)$ and $\hat{\boldsymbol{\alpha}} = (\hat{\alpha}_1, \hat{\alpha}_2, \ldots, \hat{\alpha}_C)$ with C is the number of categories. We first provide some preliminary results related to Dirichlet distribution.

The probability density function for a Dirichlet distribution for a vector $\boldsymbol{p}$ is given by:

$$D(\boldsymbol{p}|\boldsymbol{\alpha}) = \frac{1}{B(\boldsymbol{\alpha})} \prod_{i=1}^{C} p_i^{\alpha_i - 1} \tag{13}$$

where $B(\boldsymbol{\alpha})$ is the beta function for the vector $\boldsymbol{\alpha}$.

$$B(\boldsymbol{\alpha}) = \frac{\prod_{i=1}^{C} \Gamma(\alpha_i)}{\Gamma\left(\alpha_0\right)} \tag{14}$$

We use $\alpha_0 = \sum_{i=1}^{C} \alpha_i$ and $\hat{\alpha}_0 = \sum_{i=1}^{C} \hat{\alpha}_i$ for simplification.

Then, the Kullback-Leibler divergence of $\boldsymbol{p}$ from $\boldsymbol{q}$ is given by

$$\text{KL}[\boldsymbol{p} \parallel \boldsymbol{q}] = \log B(\hat{\boldsymbol{\alpha}}) - \log B(\boldsymbol{\alpha}) + \sum_{i=1}^{C} (\alpha_i - \hat{\alpha}_i) \left[\psi(\alpha_i) - \psi\left(\alpha_0\right)\right] \tag{15}$$

The entropy of $\boldsymbol{p}$ is given by:

$$H(\boldsymbol{p}) = \log B(\boldsymbol{\alpha}) + (\alpha_0 - C)\, \psi\left(\alpha_0\right) - \sum_{i=1}^{C} (\alpha_i - 1) \psi(\alpha_i) \tag{16}$$

Proposition 1. *Given a predicted distribution $\boldsymbol{p} \sim \texttt{Dir}(\boldsymbol{\alpha})$, where $\boldsymbol{\alpha} = (\alpha_1, \alpha_2, \ldots, \alpha_C)$ and C is the number of categories, and a target distribution $\boldsymbol{q} \sim \texttt{Dir}(\hat{\boldsymbol{\alpha}})$, assuming a one-hot style target distribution such that $\hat{\alpha}_i = 1$ for all $i \neq c^*$ where c^* is the ground truth label and $\hat{\alpha}_{c^*} = 2$, we have the following loss function:*

$$\mathcal{L}^{UCE} = KL(\texttt{Dir}(\boldsymbol{\alpha}) \parallel \texttt{Dir}(\hat{\boldsymbol{\alpha}})) + H(\texttt{Dir}(\boldsymbol{\alpha})) - \log(B(\hat{\boldsymbol{\alpha}})) \tag{7}$$

Proof. Combine Equation 15 and 16, then we have

$$\text{KL}(\texttt{Dir}(\boldsymbol{\alpha}) \parallel \texttt{Dir}(\hat{\boldsymbol{\alpha}})) + \text{H}(\texttt{Dir}(\boldsymbol{\alpha})) = \log B(\hat{\boldsymbol{\alpha}}) + \sum_{i=1}^{C} (\hat{\alpha}_i - 1) \left[\psi(\alpha_0) - \psi(\alpha_i)\right] \tag{17}$$

Given that $\hat{\boldsymbol{\alpha}}$ is a perfect separable target distribution, i.e. , $\hat{\alpha}_i = 1$ for all $i \neq c^*$, then we have

$$\text{KL}(\texttt{Dir}(\boldsymbol{\alpha}) \parallel \texttt{Dir}(\hat{\boldsymbol{\alpha}})) + \text{H}(\texttt{Dir}(\boldsymbol{\alpha})) = (\hat{\alpha}_{c^*} - 1) \left[\psi(\alpha_0) - \psi(\alpha_{c^*})\right] + \log B(\hat{\boldsymbol{\alpha}}) \tag{18}$$

The uncertainty cross entropy loss is the expectation of cross entropy loss, i.e.

$$\mathcal{L}^{\text{UCE}} = \mathbb{E}_{\mathbf{p} \sim \texttt{Dir}(\boldsymbol{\alpha})} \left[-\sum_{i=1}^{C} y_c \log p_c \right] = \psi(\alpha_0) - \psi(\alpha_{c^*}) \tag{19}$$

Then we have:

$$\mathcal{L}^{\text{UCE}} = \frac{\text{KL}(\texttt{Dir}(\boldsymbol{\alpha}) \parallel \texttt{Dir}(\hat{\boldsymbol{\alpha}})) + \text{H}(\texttt{Dir}(\boldsymbol{\alpha})) - \log B(\hat{\boldsymbol{\alpha}})}{\hat{\alpha}_{c^*} - 1} \tag{20}$$

$$= \frac{\text{KL}(\texttt{Dir}(\boldsymbol{\alpha}) \parallel \texttt{Dir}(\hat{\boldsymbol{\alpha}}))}{\hat{\alpha}_{c^*} - 1} + \frac{\text{H}(\texttt{Dir}(\boldsymbol{\alpha}))}{\hat{\alpha}_{c^*} - 1} + \frac{\log B(\hat{\boldsymbol{\alpha}})}{\hat{\alpha}_{c^*} - 1} \tag{21}$$

Considering the loss for a single point, the term $e_c = \alpha_c - 1$ represents the number of events that occurred given the uniform prior, with 1 being the maximum value 0 being the minimum value. Therefore, for each sample observed, we only have $\hat{\alpha}_{c^*} = e_{c^*}+1 = 2$ while $\hat{\alpha}_c = e_c+1 = 1, \forall c \neq c^*$, which corresponds to the only event occurred at ground-truth class c^*. Consequently, the loss function is given by:

$$\mathcal{L}^{\text{UCE}} = \text{KL}(\texttt{Dir}(\boldsymbol{\alpha}) \parallel \texttt{Dir}(\hat{\boldsymbol{\alpha}})) + \text{H}(\texttt{Dir}(\boldsymbol{\alpha})) - \log(B(\hat{\boldsymbol{\alpha}})) \tag{22}$$

□

Based on Proposition 1, when we minimize the UCE loss, we are minimizing the KL divergence between a predicted Dirichlet distribution with a target distribution with 'one-hot' evidence, as well as minimize the entropy of the predicted Dirichlet distribution. This will lead the Dirichlet distribution to peak at some point and can not spread to denote the true distribution, leading to overfitting.

Proposition 3. *Given a random variable $\boldsymbol{p}$ following a Dirichlet distribution $\texttt{Dir}(\boldsymbol{\alpha})$, then the expectation of Focal loss has the following analytical form:*

$$\mathcal{L}^{UFCE} = \mathbb{E}_{\boldsymbol{p}\sim Dir(\boldsymbol{\alpha})}\left[-(1-p_{c^*})^{\gamma}\log p_{c^*}\right] \tag{23}$$

$$= \frac{\Gamma(\alpha_0 - \alpha_{c^*} + \gamma)\Gamma(\alpha_0)}{\Gamma(\alpha_0 + \gamma)\Gamma(\alpha_0 - \alpha_{c^*})}\left[\psi(\alpha_0 + \gamma) - \psi(\alpha_{c^*})\right] \tag{24}$$

where $B(\cdot)$ denote Beta function and $\boldsymbol{\alpha} \in [1, +\infty)^C$ is the predicted strength parameter and C is the number of classes.

Proof. Let $B(\cdot)$ denote the Beta function and $\texttt{Beta}(\cdot)$ denote the Beta distribution. Define the Gamma function as $\Gamma(\cdot)$, the Digamma function as $\psi(\cdot)$, and the Trigamma function as $\psi_1(\cdot)$. Let $\mathbf{y}$ be the ground-truth target one-hot vector and $\mathbf{p}$ be the predicted probability distribution over the simplex Δ. For simplicity, denote c^* as the index of the ground-truth class and define $\alpha_0 = \sum_c \alpha_c$.

The analytical form of Uncertainty Focal Loss can be derived as

$$\begin{aligned}
\mathcal{L}^{\text{UFCE}} &= \mathbb{E}_{\mathbf{p}\sim\texttt{Dir}(\boldsymbol{\alpha})}\left[-\sum_{c=1}^{C} y_c(1-p_c)^{\gamma}\log p_c\right] \\
&= -\int (1-p_{c^*})^{\gamma}\log(p_{c^*})\texttt{Dir}(\mathbf{p}|\boldsymbol{\alpha})d\mathbf{p} \\
&= -\int (1-p_{c^*})^{\gamma}\log(p_{c^*})\texttt{Beta}(p_{c^*}|\alpha_{c^*}, \alpha_0 - \alpha_{c^*})dp_{c^*} \\
&= -\frac{1}{B(\alpha_{c^*}, \alpha_0 - \alpha_{c^*})}\int (1-p_{c^*})^{\gamma}\log(p_{c^*})p_{c^*}^{\alpha_{c^*}-1}(1-p_{c^*})^{\alpha_0-\alpha_{c^*}-1}dp_{c^*} \\
&= -\frac{1}{B(\alpha_{c^*}, \alpha_0 - \alpha_{c^*})}\int \left(\frac{d}{d\alpha_{c^*}}p_{c^*}^{\alpha_{c^*}-1}\right)(1-p_{c^*})^{\gamma}(1-p_{c^*})^{\alpha_0-\alpha_{c^*}-1}dp_{c^*} \\
&= -\frac{1}{B(\alpha_{c^*}, \alpha_0 - \alpha_{c^*})}\frac{d}{d\alpha_{c^*}}\int \left[(1-p_{c^*})^{\gamma}p_{c^*}^{\alpha_{c^*}-1}(1-p_{c^*})^{\alpha_0-\alpha_{c^*}-1}\right]dp_{c^*} \\
&= -\frac{1}{B(\alpha_{c^*}, \alpha_0 - \alpha_{c^*})}\frac{d}{d\alpha_{c^*}}\int \left[p_{c^*}^{\alpha_{c^*}-1}(1-p_{c^*})^{\alpha_0-\alpha_{c^*}+\gamma-1}\right]dp_{c^*} \\
&= -\frac{1}{B(\alpha_{c^*}, \alpha_0 - \alpha_{c^*})}\frac{d}{d\alpha_{c^*}}B(\alpha_{c^*}, \alpha_0 - \alpha_{c^*} + \gamma) \\
&= -\frac{1}{B(\alpha_{c^*}, \alpha_0 - \alpha_{c^*})}\frac{d}{d\alpha_{c^*}}\frac{\Gamma(\alpha_{c^*})\Gamma(\alpha_0 - \alpha_{c^*} + \gamma)}{\Gamma(\alpha_0 + \gamma)} \\
&= -\frac{1}{B(\alpha_{c^*}, \alpha_0 - \alpha_{c^*})}B(\alpha_{c^*}, \alpha_0 - \alpha_{c^*} + \gamma)\left[\psi(\alpha_{c^*}) - \psi(\alpha_0 + \gamma)\right] \\
&= \frac{\Gamma(\alpha_{c^*})\Gamma(\alpha_0 - \alpha_{c^*} + \gamma)/\Gamma(\alpha_0 + \gamma)}{\Gamma(\alpha_{c^*})\Gamma(\alpha_0 - \alpha_{c^*})/\Gamma(\alpha_0)}\left[\psi(\alpha_0 + \gamma) - \psi(\alpha_{c^*})\right] \\
&= \frac{\Gamma(\alpha_0)\Gamma(\alpha_0 - \alpha_{c^*} + \gamma)}{\Gamma(\alpha_0 + \gamma)\Gamma(\alpha_0 - \alpha_{c^*})}\left[\psi(\alpha_0 + \gamma) - \psi(\alpha_{c^*})\right].
\end{aligned} \tag{25}$$

□

Proposition 4. *Given that $\gamma \geq 1$, the UFCE loss has the lower bound involving UCE loss as:*

$$\mathcal{L}^{UFCE} \geq \mathcal{L}^{UCE} - \gamma \cdot \mathbb{E}_{\mathbf{p}\sim\texttt{Dir}(\boldsymbol{\alpha})}\Big[H(\mathbf{p})\Big]. \tag{26}$$

Proof. For any $\gamma \geq 1$, by applying Bernoulli's inequality and Hölder's inequality, we have the following relation when having the same predicted $\boldsymbol{\alpha}$:

$$\begin{aligned}
\mathcal{L}^{\text{UFCE}} &= \mathbb{E}_{\mathbf{p}\sim\texttt{Dir}(\boldsymbol{\alpha})}\Big[-\sum_{c=1}^{C}(1-p_c)^{\gamma}y_c\log(p_c)\Big] \\
&\geq \mathbb{E}_{\mathbf{p}\sim\texttt{Dir}(\boldsymbol{\alpha})}\Big[-\sum_{c=1}^{C}(1-\gamma\cdot p_c)y_c\log(p_c)\Big] \\
&= \mathbb{E}_{\mathbf{p}\sim\texttt{Dir}(\boldsymbol{\alpha})}\Big[-\sum_{c=1}^{C}y_c\log(p_c)+\sum_{c=1}^{C}\gamma y_c p_c\log(p_c)\Big] \\
&= \mathbb{E}_{\mathbf{p}\sim\texttt{Dir}(\boldsymbol{\alpha})}\Big[-\sum_{c=1}^{C}y_c\log(p_c)-\Big|\sum_{c=1}^{C}\gamma y_c p_c\log(p_c)\Big|\Big] \\
&= \mathbb{E}_{\mathbf{p}\sim\texttt{Dir}(\boldsymbol{\alpha})}\Big[-\sum_{c=1}^{C}y_c\log(p_c)-\gamma\Big\|\mathbf{y}^{\top}(\mathbf{p}\circ\log(\mathbf{p}))\Big\|_1\Big] \\
&\geq \mathbb{E}_{\mathbf{p}\sim\texttt{Dir}(\boldsymbol{\alpha})}\Big[-\sum_{c=1}^{C}y_c\log(p_c)-\gamma\|\mathbf{y}\|_{\infty}\|\mathbf{p}\circ\log(\mathbf{p})\|_1\Big] \\
&= \mathbb{E}_{\mathbf{p}\sim\texttt{Dir}(\boldsymbol{\alpha})}\Big[-\sum_{c=1}^{C}y_c\log(p_c)-\gamma\Big(\max_j y_j\Big)\Big|\sum_{c=1}^{C}p_c\log(p_c)\Big|\Big] \\
&= \mathbb{E}_{\mathbf{p}\sim\texttt{Dir}(\boldsymbol{\alpha})}\Big[-\sum_{c=1}^{C}y_c\log(p_c)-\gamma\Big|\sum_{c=1}^{C}p_c\log(p_c)\Big|\Big] \\
&= \mathbb{E}_{\mathbf{p}\sim\texttt{Dir}(\boldsymbol{\alpha})}\Big[-\sum_{c=1}^{C}y_c\log(p_c)\Big]-\gamma\cdot\mathbb{E}_{\mathbf{p}\sim\texttt{Dir}(\boldsymbol{\alpha})}\Big[-\sum_{c=1}^{C}p_c\log(p_c)\Big] \\
&= \mathbb{E}_{\mathbf{p}\sim\texttt{Dir}(\boldsymbol{\alpha})}\Big[-\sum_{c=1}^{C}y_c\log(p_c)\Big]-\gamma\cdot\mathbb{E}_{\mathbf{p}\sim\texttt{Dir}(\boldsymbol{\alpha})}\Big[H(\mathbf{p})\Big] \\
&= \mathcal{L}^{\text{UCE}}-\gamma\cdot\mathbb{E}_{\mathbf{p}\sim\texttt{Dir}(\boldsymbol{\alpha})}\Big[H(\mathbf{p})\Big],
\end{aligned} \tag{27}$$

□

where $\circ$ denotes element-wise product.

Proposition 4 shows that the lower bound of UFCE loss is equivalent to the UCE loss minus the entropy where γ is a trade-off parameter.

Proposition 5. *For uncertainty focal loss $\mathcal{L}^{UFCE}$, the partial derivative with respect to the ground truth class c^* has the form:*

$$\frac{\partial}{\partial\alpha_{c^*}}\mathcal{L}^{UFCE} = \frac{\Gamma(\alpha_0)\Gamma(\alpha_0-\alpha_{c^*}+\gamma)}{\Gamma(\alpha_0+\gamma)\Gamma(\alpha_0-\alpha_{c^*})}\Bigg\{\Big[\psi(\alpha_0)-\psi(\alpha_0+\gamma)\Big]\cdot\Big[\psi(\alpha_0+\gamma)-\psi(\alpha_{c^*})\Big] \tag{28}$$

$$+\Big[\psi_1(\alpha_0+\gamma)-\psi_1(\alpha_{c^*})\Big]\Bigg\}. \tag{29}$$

Proof. for UFCE loss, the gradient is

$$\begin{aligned}
\frac{\partial}{\partial \alpha_{c^*}} \mathcal{L}^{\text{UFCE}} &= \frac{\partial}{\partial \alpha_{c^*}} \left[\frac{\Gamma(\alpha_0)\Gamma(\alpha_0 - \alpha_{c^*} + \gamma)}{\Gamma(\alpha_0 + \gamma)\Gamma(\alpha_0 - \alpha_{c^*})} \cdot [\psi(\alpha_0 + \gamma) - \psi(\alpha_{c^*})] \right] \\
&= \left[\frac{\partial}{\partial \alpha_{c^*}} \frac{B(\alpha_0, \gamma)}{B(\alpha_0 - \alpha_{c^*}, \gamma)} \right] \cdot [\psi(\alpha_0 + \gamma) - \psi(\alpha_{c^*})] \\
&\quad + \frac{B(\alpha_0, \gamma)}{B(\alpha_0 - \alpha_{c^*}, \gamma)} \cdot \frac{\partial}{\partial \alpha_{c^*}} \left[\psi(\alpha_0 + \gamma) - \psi(\alpha_{c^*}) \right] \\
&= \left[\frac{B(\alpha_0, \gamma)}{B(\alpha_0 - \alpha_{c^*}, \gamma)} \right] \cdot [\psi(\alpha_0) - \psi(\alpha_0 + \gamma)] \cdot [\psi(\alpha_0 + \gamma) - \psi(\alpha_{c^*})] \\
&\quad + \frac{B(\alpha_0, \gamma)}{B(\alpha_0 - \alpha_{c^*}, \gamma)} \cdot \left[\psi_1(\alpha_0 + \gamma) - \psi_1(\alpha_{c^*}) \right] \\
&= \frac{\Gamma(\alpha_0)\Gamma(\alpha_0 - \alpha_{c^*} + \gamma)}{\Gamma(\alpha_0 + \gamma)\Gamma(\alpha_0 - \alpha_{c^*})} \Bigg\{ \left[\psi(\alpha_0) - \psi(\alpha_0 + \gamma) \right] \cdot \left[\psi(\alpha_0 + \gamma) - \psi(\alpha_{c^*}) \right] \\
&\quad + \left[\psi_1(\alpha_0 + \gamma) - \psi_1(\alpha_{c^*}) \right] \Bigg\}.
\end{aligned} \tag{30}$$

□

In the following proposition, we consider the influence of gradients on the prediction of α_{c^*}. Let $\mathbf{w}_{c^*}$ denote the vector of weight parameters in the last linear layer that influences the prediction of the true-class evidence c^*. Let $\mathbf{s}$ denote the logits and $\mathbf{z}$ be the input to the last linear layer. The prediction of α_{c^*} has the following form:

$$c^* = \sigma_{\text{ReLU}} \left(\mathbf{w}_{c^*}^T \begin{bmatrix} \mathbf{z} \\ 1 \end{bmatrix} \right),$$

where the last weight in $\mathbf{w}_{c^*}$ is related to the intercept.

Proposition 2. *Comparing $\mathcal{L}^{UFCE}$ and $\mathcal{L}^{UCE}$ with numerical analysis on the gradient of the parameters $\mathbf{w}_{c^*}$ in the last linear layer, we have,*

$$\left\| \frac{\partial \mathcal{L}^{UFCE}}{\partial \mathbf{w}_{c^*}} \right\| - \left\| \frac{\partial \mathcal{L}^{UCE}}{\partial \mathbf{w}_{c^*}} \right\| \begin{cases} \geq 0 & \text{if } \bar{p}_{c^*} \leq \tau_1(\alpha_{c^*}, \gamma) \\ < 0 & \text{if } \bar{p}_{c^*} > \tau_2(\alpha_{c^*}, \gamma) \end{cases},$$

where $\tau_1(\alpha_{c^*}, \gamma)$ and $\tau_2(\alpha_{c^*}, \gamma)$ are two thresholds within $(\frac{1}{\alpha_0}, 1 - \frac{1}{\alpha_0})$. respectively.

Proof. Define $\mathbf{w}_{c^*}$ as the model parameter of the last linear layer. Using the chain rule, we can easily derive the gradient for the last linear layer's parameter:

$$\begin{aligned}
\frac{\partial \mathcal{L}^{\text{UFCE}}}{\partial \mathbf{w}_{c^*}} &= \left(\frac{\partial \mathbf{s}}{\partial \mathbf{w}_{c^*}} \right) \left(\frac{\partial \alpha_c}{\partial \mathbf{s}} \right) \left(\frac{\partial \mathcal{L}^{\text{UFCE}}}{\partial \alpha_{c^*}} \right), \\
\frac{\partial \mathcal{L}^{\text{UCE}}}{\partial \mathbf{w}_{c^*}} &= \left(\frac{\partial \mathbf{s}}{\partial \mathbf{w}_{c^*}} \right) \left(\frac{\partial \alpha_c}{\partial \mathbf{s}} \right) \left(\frac{\partial \mathcal{L}^{\text{UCE}}}{\partial \alpha_{c^*}} \right).
\end{aligned} \tag{31}$$

This establishes a connection between the gradient of the last layer's weight and the gradient of the loss functions with respect to α_{c^*}. Thus, $\left\| \frac{\partial \mathcal{L}^{\text{UFCE}}}{\partial \alpha_c} \right\| - \left\| \frac{\partial \mathcal{L}^{\text{UCE}}}{\partial \alpha_c} \right\|$ implies $\left\| \frac{\partial \mathcal{L}^{\text{UFCE}}}{\partial \mathbf{w}_{c^*}} \right\| - \left\| \frac{\partial \mathcal{L}^{\text{UCE}}}{\partial \mathbf{w}_{c^*}} \right\|$.

The uncertainty cross entropy loss is given by:

$$\mathcal{L}^{\text{UCE}} = \mathbb{E}_{\mathbf{p} \sim \texttt{Dir}(\boldsymbol{\alpha})} \left[-\sum_{c=1}^{C} y_c \log p_c \right] = \sum_{c=1}^{C} y_c \left[\psi(\alpha_0) - \psi(\alpha_c) \right] = \psi(\alpha_0) - \psi(\alpha_{c^*}) \tag{32}$$

Its gradient is given by the difference of trigamma functions:

$$\frac{\partial \mathcal{L}^{\text{UCE}}}{\partial \alpha_{c^*}} = \psi_1(\alpha_0) - \psi_1(\alpha_{c^*}). \tag{33}$$

According to Proposition 5, we have:

$$\frac{\partial \mathcal{L}^{\text{UFCE}}}{\partial \alpha_{c^*}} = \frac{\Gamma(\alpha_0)\Gamma(\alpha_0 - \alpha_{c^*} + \gamma)}{\Gamma(\alpha_0 + \gamma)\Gamma(\alpha_0 - \alpha_{c^*})} \left\{ [\psi(\alpha_0) - \psi(\alpha_0 + \gamma)] [\psi(\alpha_0 + \gamma) - \psi(\alpha_{c^*})] + [\psi_1(\alpha_0 + \gamma) - \psi_1(\alpha_{c^*})] \right\}.$$

The difference between the l1-norm of gradients is:

$$\left| \frac{\partial \mathcal{L}^{\text{UFCE}}}{\partial \alpha_0} \right| - \left| \frac{\partial \mathcal{L}^{\text{UCE}}}{\partial \alpha_0} \right| = -\frac{\Gamma(\alpha_0)\Gamma(\alpha_0 - \alpha_{c^*} + \gamma)}{\Gamma(\alpha_0 + \gamma)\Gamma(\alpha_0 - \alpha_{c^*})} \Big\{ [\psi(\alpha_0) - \psi(\alpha_0 + \gamma)] [\psi(\alpha_0 + \gamma) - \psi(\alpha_{c^*})] + [\psi_1(\alpha_0 + \gamma) - \psi_1(\alpha_{c^*})] \Big\} + (\psi_1(\alpha_0) - \psi_1(\alpha_{c^*})), \quad (34)$$

where $\frac{\partial \mathcal{L}^{\text{UFCE}}}{\partial \alpha_0}$ and $\frac{\partial \mathcal{L}^{\text{UCE}}}{\partial \alpha_0}$ can be shown to be negative for all $\alpha_0 > 2$, $\alpha_{c^*} > 1$, and $\gamma \in [0, 5]$.

Let $\bar{p}_{c^*} = \frac{\alpha_{c^*}}{\alpha_0}$ and $\alpha_{c^*} = \bar{p}_{c^*}\alpha_0$. We now analyze the relation between the difference and the projected class probability term $\bar{p}_{c^*}$. Rewriting the difference based on $\bar{p}_{c^*}$, we denote the resulting form as $f(\bar{p}_{c^*}, \alpha_0, \gamma)$:

$$f(\bar{p}_{c^*}, \alpha_0, \gamma) = -\frac{\Gamma(\alpha_0)\Gamma(\alpha_0 - \bar{p}_{c^*}\alpha_0 + \gamma)}{\Gamma(\alpha_0 + \gamma)\Gamma(\alpha_0 - \bar{p}_{c^*}\alpha_0)} \Big\{ [\psi(\alpha_0) - \psi(\alpha_0 + \gamma)] [\psi(\alpha_0 + \gamma) - \psi(\bar{p}_{c^*}\alpha_0)] + [\psi_1(\alpha_0 + \gamma) - \psi_1(\bar{p}_{c^*}\alpha_0)] \Big\} + (\psi_1(\alpha_0) - \psi_1(\bar{p}_{c^*}\alpha_0)).$$

Next, we derive the gradient of this difference function with respect to $\bar{p}_{c^*}$. Let:

$$A(\bar{p}_{c^*}) = \frac{\Gamma(\alpha_0)\Gamma(\alpha_0 - \bar{p}_{c^*}\alpha_0 + \gamma)}{\Gamma(\alpha_0 + \gamma)\Gamma(\alpha_0 - \bar{p}_{c^*}\alpha_0)},$$

$$B(\bar{p}_{c^*}) = [\psi(\alpha_0) - \psi(\alpha_0 + \gamma)] [\psi(\alpha_0 + \gamma) - \psi(\bar{p}_{c^*}\alpha_0)] + [\psi_1(\alpha_0 + \gamma) - \psi_1(\bar{p}_{c^*}\alpha_0)].$$

Then,

$$f(\bar{p}_{c^*}; \alpha_0, \gamma) = -A(\bar{p}_{c^*})B(\bar{p}_{c^*}) + (\psi_1(\alpha_0) - \psi_1(\bar{p}_{c^*}\alpha_0)).$$

First, we find $\frac{\partial A(\bar{p}_{c^*})}{\partial \bar{p}_{c^*}}$. Recall that the derivative of the Gamma function with respect to its argument is: $\frac{d}{dz}\Gamma(z) = \Gamma(z)\psi(z)$. Using the product rule and the chain rule:

$$\begin{aligned}
\frac{\partial A(\bar{p}_{c^*})}{\partial \bar{p}_{c^*}} &= \frac{\Gamma(\alpha_0)}{\Gamma(\alpha_0 + \gamma)} \left[\frac{d}{d\bar{p}_{c^*}} \left(\frac{\Gamma(\alpha_0 - \bar{p}_{c^*}\alpha_0 + \gamma)}{\Gamma(\alpha_0 - \bar{p}_{c^*}\alpha_0)} \right) \right] \\
&= \frac{\Gamma(\alpha_0)}{\Gamma(\alpha_0 + \gamma)} \left[\frac{d}{d\bar{p}_{c^*}} \frac{\Gamma(\alpha_0 - \bar{p}_{c^*}\alpha_0 + \gamma) [-\alpha_0\psi(\alpha_0 - \bar{p}_{c^*}\alpha_0 + \gamma) + \alpha_0\psi(\alpha_0 - \bar{p}_{c^*}\alpha_0)]}{\Gamma(\alpha_0 - \bar{p}_{c^*}\alpha_0)} \right] \\
&= \frac{\Gamma(\alpha_0 - \bar{p}_{c^*}\alpha_0 + \gamma)}{\Gamma(\alpha_0 - \bar{p}_{c^*}\alpha_0)} [-\alpha_0\psi(\alpha_0 - \bar{p}_{c^*}\alpha_0 + \gamma) + \alpha_0\psi(\alpha_0 - \bar{p}_{c^*}\alpha_0)] \\
&= A(\bar{p}_{c^*}) [-\alpha_0\psi(\alpha_0 - \bar{p}_{c^*}\alpha_0 + \gamma) + \alpha_0\psi(\alpha_0 - \bar{p}_{c^*}\alpha_0)].
\end{aligned} \quad (35)$$

Next, we find $\frac{\partial B(p)}{\partial \bar{p}_{c^*}}$:

$$\frac{\partial B(\bar{p}_{c^*})}{\partial \bar{p}_{c^*}} = [\psi(\alpha_0) - \psi(\alpha_0 + \gamma)] [-\alpha_0\psi_1(\bar{p}_{c^*}\alpha_0)] + [-\alpha_0\psi_2(\bar{p}_{c^*}\alpha_0)]. \quad (36)$$

Then, we find the total derivative of $f(\bar{p}_{c^*}; \alpha_0, \gamma)$:

$$\begin{aligned}
\frac{\partial f(\bar{p}_{c^*}; \alpha_0, \gamma)}{\partial \bar{p}_{c^*}} &= -\frac{\partial A(\bar{p}_{c^*})}{\partial \bar{p}_{c^*}} B(\bar{p}_{c^*}) - A(\bar{p}_{c^*}) \frac{\partial B(\bar{p}_{c^*})}{\partial \bar{p}_{c^*}} + (-\alpha_0\psi_2(\bar{p}_{c^*}\alpha_0)) \\
&= -A(\bar{p}_{c^*}) [-\alpha_0\psi(\alpha_0 - \bar{p}_{c^*}\alpha_0 + \gamma) + \alpha_0\psi(\alpha_0 - \bar{p}_{c^*}\alpha_0)] B(\bar{p}_{c^*}) \\
&\quad - A(\bar{p}_{c^*}) [[\psi(\alpha_0) - \psi(\alpha_0 + \gamma)] [-\alpha_0\psi_1(\bar{p}_{c^*}\alpha_0)] + [-\alpha_0\psi_2(\bar{p}_{c^*}\alpha_0)]] \\
&\quad - \alpha_0\psi_2(\bar{p}_{c^*}\alpha_0) \\
&= A(\bar{p}_{c^*})\alpha_0 [\psi(\alpha_0 - \bar{p}_{c^*}\alpha_0 + \gamma) - \psi(\alpha_0 - \bar{p}_{c^*}\alpha_0)] B(\bar{p}_{c^*}) \\
&\quad - A(\bar{p}_{c^*})\alpha_0 [[\psi(\alpha_0) - \psi(\alpha_0 + \gamma)] \psi_1(\bar{p}_{c^*}\alpha_0) + \psi_2(\bar{p}_{c^*}\alpha_0)] - \alpha_0\psi_2(\bar{p}_{c^*}\alpha_0).
\end{aligned} \quad (37)$$

Noting that this derivative involves polynomial terms of polygamma functions, which are differentiable on $(0, +\infty)$, this verifies $f(\cdot)$ is also differentiable on $(0, +\infty)$. Given that $\alpha_0 \geq \alpha_{c^*} + 1$ and $\alpha_{c^*} \geq 1$, the feature range of $\bar{p}_{c^*}$ is $\left(\frac{1}{\alpha_0}, 1 - \frac{1}{\alpha_0}\right)$, $f(\cdot)$ remains differentiable in this interval. We demonstrate that $\frac{\partial f(\bar{p}_{c^*};\alpha_0,\gamma)}{\partial \bar{p}_{c^*}}$ is positive and negative at the bounding points of this range, respectively. According to the intermediate-value theorem, there exists at least one configuration of $\bar{p}_{c^*}$ in this range such that $\frac{\partial f(\bar{p}_{c^*};\alpha_0,\gamma)}{\partial \bar{p}_{c^*}} = 0$. Therefore, there exist two thresholds $\tau_1(\alpha_{c^*}, \gamma)$ and $\tau_2(\alpha_{c^*}, \gamma)$ within $\left(\frac{1}{\alpha_0}, 1 - \frac{1}{\alpha_0}\right)$, such that $\left|\frac{\partial \mathcal{L}^{\text{UFCE}}}{\partial \alpha_{c^*}}\right| > \left|\frac{\partial \mathcal{L}^{\text{UCE}}}{\partial \alpha_{c^*}}\right|$ when $\bar{p}_{c^*} < \tau_1(\alpha_{c^*}, \gamma)$, and $\left|\frac{\partial \mathcal{L}^{\text{UFCE}}}{\partial \alpha_{c^*}}\right| < \left|\frac{\partial \mathcal{L}^{\text{UCE}}}{\partial \alpha_{c^*}}\right|$ when $\bar{p}_{c^*} > \tau_2(\alpha_{c^*}, \gamma)$.

First, substitute $\bar{p}_{c^*} = \frac{1}{\alpha_0}$:

$$
\begin{aligned}
f\left(\frac{1}{\alpha_0}; \alpha_0, \gamma\right) = -\frac{\Gamma(\alpha_0)\Gamma(\alpha_0 - 1 + \gamma)}{\Gamma(\alpha_0 + \gamma)\Gamma(\alpha_0 - 1)} \Big\{ & \left[\psi(\alpha_0) - \psi(\alpha_0 + \gamma)\right] \left[\psi(\alpha_0 + \gamma) - \psi(1)\right] \\
& + \left[\psi_1(\alpha_0 + \gamma) - \psi_1(1)\right] \Big\} + \left(\psi_1(\alpha_0) - \psi_1(1)\right).
\end{aligned} \tag{38}
$$

Using the properties of the Gamma function, $\Gamma(\alpha_0 - 1) = \frac{\Gamma(\alpha_0)}{\alpha_0 - 1}$ and $\psi(1) = -\gamma_E$ and $\psi_1(1) = \frac{\pi^2}{6}$, where γ_E is the Euler-Mascheroni constant, the expression simplifies to:

$$
\begin{aligned}
f\left(\frac{1}{\alpha_0}; \alpha_0, \gamma\right) &= -\frac{\alpha_0 - 1}{\alpha_0 + \gamma - 1} \Big\{ \left[\psi(\alpha_0) - \psi(\alpha_0 + \gamma)\right] \left[\psi(\alpha_0 + \gamma) - \psi(1)\right] \\
&\quad + \left[\psi_1(\alpha_0 + \gamma) - \psi_1(1)\right] \Big\} + \left(\psi_1(\alpha_0) - \psi_1(1)\right) \\
&= -\frac{\alpha_0 - 1}{\alpha_0 + \gamma - 1} \Big\{ \left[\psi(\alpha_0) - \psi(\alpha_0 + \gamma)\right] \left[\psi(\alpha_0 + \gamma) + \gamma_E\right] \\
&\quad + \left[\psi_1(\alpha_0 + \gamma) - \frac{\pi^2}{6}\right] \Big\} + \left(\psi_1(\alpha_0) - \frac{\pi^2}{6}\right).
\end{aligned} \tag{39}
$$

It is evident from numerical analysis that $f\left(\frac{1}{\alpha_0}; \alpha_0, \gamma\right) > 0$ for all $\gamma \in [0, 5]$ and $\alpha_0 > 2$.

Substituting $\bar{p}_{c^*} = 1 - \frac{1}{\alpha_0}$, we have

$$
\begin{aligned}
f\left(1 - \frac{1}{\alpha_0}; \alpha_0, \gamma\right) = -\frac{\Gamma(\alpha_0)\Gamma(1 + \gamma)}{\Gamma(\alpha_0 + \gamma)\Gamma(1)} \Big\{ & \left[\psi(\alpha_0) - \psi(\alpha_0 + \gamma)\right] \left[\psi(\alpha_0 + \gamma) - \psi(\alpha_0 - 1)\right] \\
& + \left[\psi_1(\alpha_0 + \gamma) - \psi_1(\alpha_0 - 1)\right] \Big\} + \left(\psi_1(\alpha_0) - \psi_1(\alpha_0 - 1)\right).
\end{aligned} \tag{40}
$$

It is evident from numerical analysis that $f\left(1 - \frac{1}{\alpha_0}; \alpha_0, \gamma\right) < 0$ for all $\gamma \in [0, 5]$ and $\alpha_0 > 2$.

□

A.2 Related Work

A.2.1 Vision-based Bird's eye view semantic segmentation

Bird's-eye view (BEV) serves as an effective representation for fusing information from multiple cameras, making it a central component in autonomous driving systems. However, transforming camera images into BEV maps presents significant challenges, primarily due to the complexity of depth estimation and 3D geometric transformations. The key component of BEVSS is the 2D-to-3D lifting strategy, which employs techniques such as depth-weighted splitting (Philion & Fidler, 2020; Hu et al., 2021), attention mechanisms (Zhou & Krähenbühl, 2022), and bilinear sampling (Harley et al., 2023).

In this paper, we use three representative methods, Lift splat shoot (LSS) (Philion & Fidler, 2020), Cross-View Transformer (CVT) (Zhou & Krähenbühl, 2022), and Simple-BEV (Harley et al., 2023).

Figure 2: Numerical analysis of $\left\| \frac{\partial \mathcal{L}^{\text{Ufce}}}{\partial \mathbf{w}_{c^*}} \right\| - \left\| \frac{\partial \mathcal{L}^{\text{Uce}}}{\partial \mathbf{w}_{c^*}} \right\|$ for different composition of α_{c^*} and γ

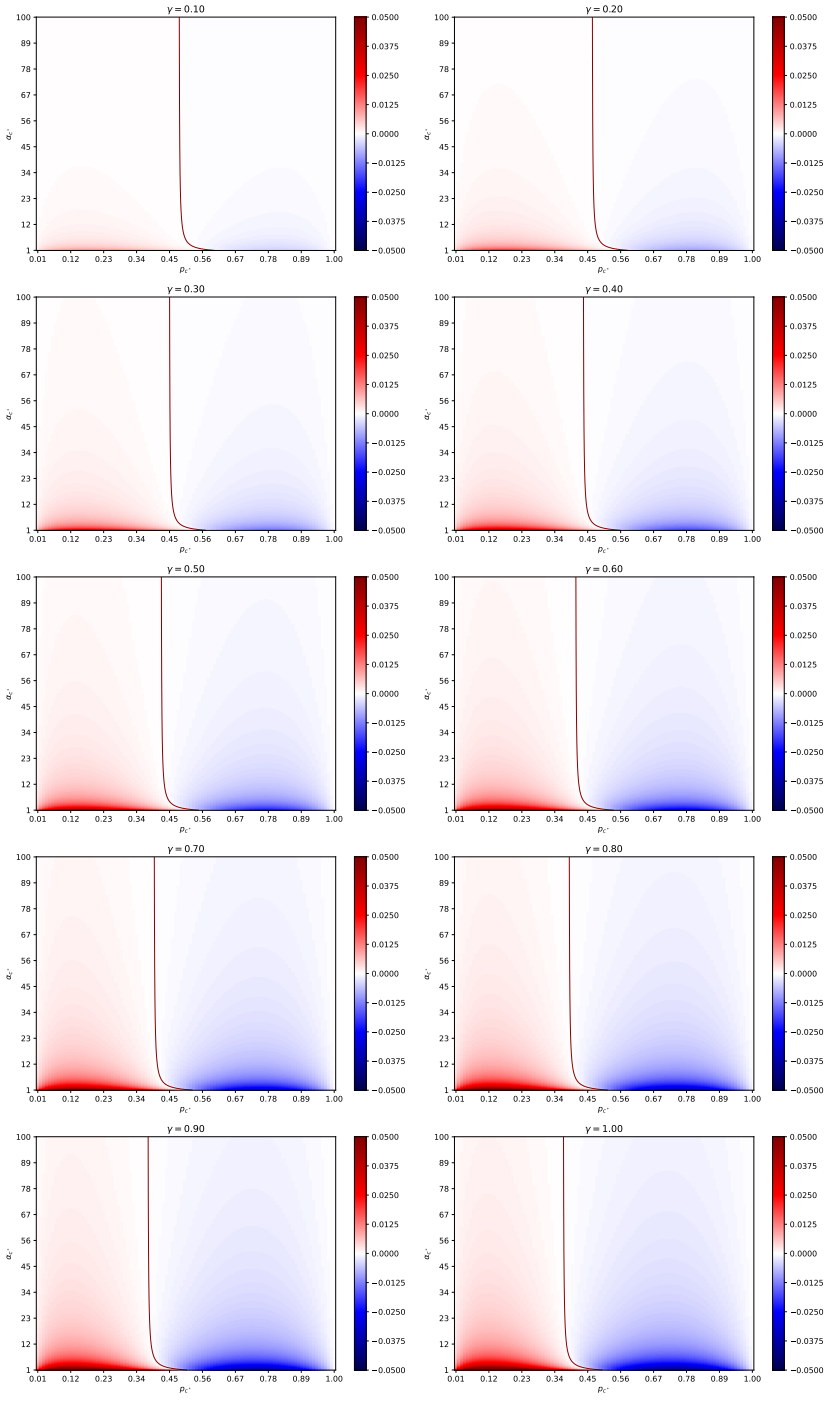

Figure 3: Implicit weight regularization impact by UFCE with $\alpha_{c^*} = 10$

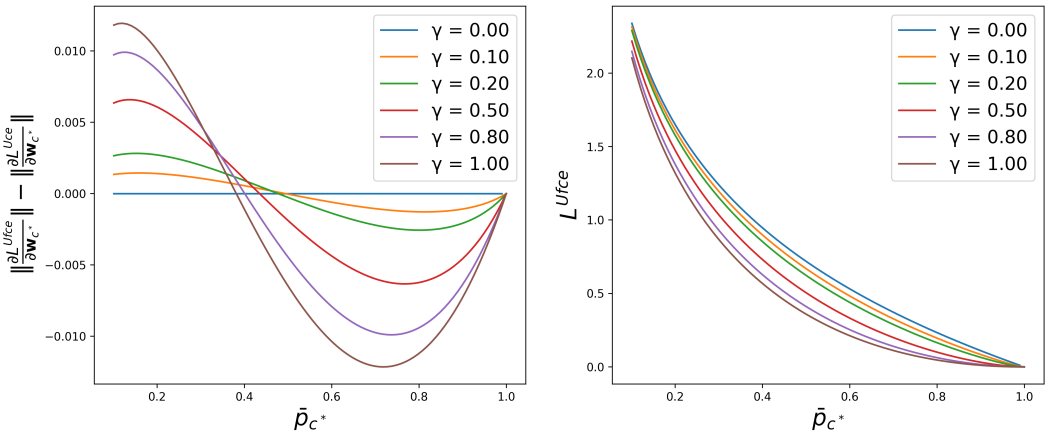

LSS leverages raw pixel inputs from multiple surrounding cameras and "lifts" each image individually into a frustum of features. Initially, it predicts a categorical distribution over a predefined set of possible depths. Subsequently, the frustum of features is generated by multiplying the features with their predicted depth probability. By utilizing known camera calibration matrices for each camera, a point cloud of features in the ego coordinate space can be obtained. LSS then "splats" all the frustums into a rasterized bird's-eye-view grid using a PointPillar (Lang et al., 2018) model. These splatted features are then fed into a decoder module to predict BEVSS. The concept of transforming from camera pixels to 3D point clouds and subsequently to BEV pixels has inspired several subsequent models, such as BEVDet (Huang et al., 2021) and FIERY (Hu et al., 2021).

CVT takes a distinct approach by leveraging transformer architecture and cross-attention mechanism. CVT begins by extracting features from multiple surrounding camera images using a pre-trained EfficientNet-B4(Tan & Le, 2019) model. These extracted features serve as the attention values in the subsequent cross-attention step. To create the attention keys, the features are concatenated with the camera-aware positional embedding. This positional embedding is constructed using known camera pose and intrinsic information, enabling the model to account for the specific characteristics of each camera. The positional encoding of the BEV space serves as the queries during the cross attention process.

Simple-BEV simplifies the process of generating BEV representations by avoiding the use of estimated depth maps. Instead, it defines a 3D coordinate volume over the BEV plane and projects each coordinate into the corresponding camera images. Image features are then sampled from the surrounding regions of the projected locations. While the resulting features are not precisely aligned in the BEV space and are distributed across potential locations, this approach significantly enhances efficiency and robustness to projection errors. PointBEV (Chambon et al., 2024) further improves the 'feature pulling' strategy with the sparse representations.

A.2.2 Uncertainty quantification on Bird's eye view semantic segmentation

To the best of our knowledge, there is no pioneer work on the uncertainty quantification on the BEVSS task. We introduce the most relative literature in the section.

Uncertainty quantification in camera view's semantic segmentation. Uncertainty quantification in pixel-level camera semantic segmentation is the most relevant research task. Similarly, uncertainty in this task also arises from two primary sources: aleatoric uncertainty, which reflects inherent ambiguity in the data (e.g., sensor noise or occlusions), and epistemic uncertainty, which represents the model's lack of knowledge due to limited or biased training data. Mukhoti & Gal (2018) evaluated Bayesian deep learning methods, including MC Dropout and Concrete Dropout, applied to semantic segmentation and introduced new patch-based evaluation metrics. However, these metrics focused on the relationship between accuracy and uncertainty, limited to aleatoric uncertainty, and

Bayesian-based approaches require multiple forward passes, making it impractical for real-time applications such as autonomous driving. Mukhoti et al. (2021) proposed single-pass uncertainty estimation by extending deep deterministic uncertainty to semantic segmentation tasks. They used Gaussian Discriminant Analysis (GDA) to model feature space means and covariance matrices per class, enabling the quantification of epistemic uncertainty through feature densities, while aleatoric uncertainty was estimated via the softmax distribution. However, this work did not provide a comprehensive quantitative evaluation of the quality of the estimated epistemic uncertainty. Ancha et al. (2024) advanced uncertainty estimation with a model based on the evidential deep learning framework. Their approach is built on a natural posterior network that estimates a pixel-level Dirichlet distribution with a density estimator based on a GMM-enhanced normalizing flow and linear classifier. To mitigate feature collapsing issues, they introduced a decoder that reconstructs image patches from pixel-level latent features. The proposed model is evaluated from both calibration view and OOD detection-like tasks.

Fusing camera view uncertainties to BEV space: Challenges and Opportunities. Uncertainty quantification in BEV semantic segmentation (BEVSS) lacks established literature, and extending methods from the camera space to BEV is non-trivial. To illustrate this challenge, we conducted a simple experiment. Using the CARLA dataset, we trained an Evidential Neural Network (ENN) model based on DeepLabV3 to quantify pixel-level uncertainty in camera images. The predicted uncertainty was then mapped from the camera space to the BEV space using a ground truth mapping function, with animals included as the OOD category. Experimental results showed an average AUPR of 47% in the camera space, but only 7% in the BEV space.

This discrepancy arises possibly because the predicted OOD regions are often larger than the actual objects. When mapped to BEV, these over-predicted regions expand further due to perspective distortion. Conversely, correctly predicted regions are restricted to the visible parts of the object, resulting in significant inaccuracies and poor performance in BEV. Finally, we highlight that incorporating camera-view uncertainties can enhance the quality of uncertainty quantification in BEV, offering a promising direction for future research.

Robutness in bird's eye view semantic segmentation. OOD robustness in BEV semantic segmentation focuses on maintaining model performance under novel and unexpected conditions, such as varying weather, lighting changes, or sensor malfunctions. RoboBEV Xie et al. (2024) provides an extensive benchmark for evaluating the robustness of BEV perception models in autonomous driving, testing their performance under various natural corruptions. For instance, they demonstrate significant performance drops in segmentation tasks when evaluating the CVT model trained on clean datasets against corrupted datasets.

We further clarify the distinction between OOD robustness and OOD detection within our experimental context. OOD robustness (or generalization) aims to ensure that models maintain high performance on OOD samples with domain shifts. In contrast, OOD detection emphasizes model reliability by identifying samples with semantic shifts—cases where the model cannot or should not generalize. Importantly, these concepts can be complementary: an uncertainty-aware model should also be robust to domain shifts, meaning it must maintain effective OOD detection even under conditions of domain shift.

Calibration in bird's eye view semantic segmentation. There indeed several works focus primarily on calibration while neglecting challenges such as out-of-distribution data and dataset shifts, which require epistemic uncertainty estimation. Kängsepp & Kull (2022) focus on overconfident probability estimates in semantic segmentation issue by applying isotonic regression for pixel-wise calibration and beta calibration for object-wise calibration. This method improves confidence reliability but does not explicitly address epistemic uncertainty. MapPrior (Zhu et al., 2023) integrates a generative prior with traditional discriminative BEV models to enhance BEV semantic segmentation performance while focusing on calibration, particularly aleatoric uncertainty. It combines an initial noisy BEV layout estimate from a predictive model with a generative refinement stage that samples diverse outputs from a transformer-based latent space. However, MapPrior's approach is limited to aleatoric uncertainty and relies on an additional model architecture, making it less adaptable to other BEV semantic segmentation models.

Uncertainty quantification on downstream tasks. Several works have explored uncertainty in downstream tasks that use bird's-eye view (BEV) maps as intermediate representations. However,

these work are also limited to calibration. UAP (Dewangan et al., 2023) targets motion planning and trajectory optimization by building an uncertainty-aware occupancy grid map. It estimates collision probabilities based on sampled distances to nearby occupied cells and optimizes trajectories using a sampling-based approach, incorporating uncertainty into the planning process. Fervers et al. (2023) focus on metric cross-view geolocalization (CVGL), which aims to localize ground-based vehicles relative to aerial map images. Their approach matches BEV representations to aerial images by predicting soft probability distributions over possible vehicle poses. The uncertainty derived from these probability distributions is integrated into a Kalman filter, improving the accuracy and robustness of trajectory tracking over time.

A.2.3 Uncertainty Quantification Baselines

Softmax-based (Hendrycks & Gimpel, 2016) Softmax entropy is one of the most commonly used metrics for uncertainty (Hendrycks & Gimpel, 2016). It is the entropy ($\mathbb{H}(p(\mathbf{Y}_{i,j}|\mathbf{X};\boldsymbol{\theta}))$) of softmax distribution $p(\mathbf{Y}_{i,j}|\mathbf{X};\boldsymbol{\theta})$.

$$\mathbb{H}(p(\mathbf{Y}_{i,j}|\mathbf{X};\boldsymbol{\theta})) = \sum\nolimits_{c=1}^{C} p_{c,i,j} \log p_{c,i,j}. \tag{41}$$

This metric is known to capture aleatoric uncertainty, but can not capture epistemic uncertainty reliably.

Energy-based (Liu et al., 2020) The energy-based model is designed to distinguish OOD data from ID data. Energy scores, which are theoretically aligned with the input's probability density, exhibit reduced susceptibility to overconfidence issues and can be considered as epistemic uncertainty. As a post-hoc method applied to predicted logits, energy scores can be flexibly utilized as a scoring function for any pre-trained neural classifier.

$$u_{i,j}^{epis} = u_{i,j}^{energy} = -T \cdot \log \sum_{c=1}^{C} \exp^{l_{c,i,j}} / T \tag{42}$$

where $l_{c,i,j}$ represents the predicted logits for pixel (i,j) associated with class c, where logits are defined as the output of the final layer prior to the softmax activation function in a standard classification model, i.e. $\mathbf{L} = f(\mathbf{X};\boldsymbol{\theta})$. T is the temperature scaling. The energy score will be employed to quantify epistemic uncertainty. There is no aleatoric uncertainty explicitly defined for energy-based models, so we use the softmax confidence score to measure aleatoric uncertainty.

$$u_{i,j}^{alea} = u_{i,j}^{conf} = -\max\nolimits_c p_{c,i,j} \tag{43}$$

Ensembles-based (Lakshminarayanan et al., 2017). Deep Ensembles-based method learn M different versions of network weights $\{\boldsymbol{\theta}^{(1)}, \cdots, \boldsymbol{\theta}^{(M)}\}$ and aggregates the predictions of these versions. The aleatoric uncertainty is measured by the softmax entropy of the mean of the predictions from different network weights. The epistemic uncertainty is measured by the variance between the model predictions.

$$\begin{aligned} u_{i,j}^{alea} &= \sum\nolimits_{c=1}^{C} \left(\frac{1}{M} \sum\nolimits_{m=1}^{M} p_{c,i,j}^{(m)} \right) \log \left(\frac{1}{M} \sum\nolimits_{m=1}^{M} p_{c,i,j}^{(m)} \right) \\ u_{i,j}^{epis} &= \text{var}(\{p_{\hat{c},i,j}^{(m)}\}_{m=1}^{M}), \quad \hat{c} = \text{argmax} \left(\frac{1}{M} \sum\nolimits_{m=1}^{M} \boldsymbol{p}_{i,j}^{(m)} \right) \end{aligned} \tag{44}$$

where $p_{i,j}^{(m)} \in [0,1]^C$ refers to the predictions of BEV network based on the network weights $\boldsymbol{\theta}^{(m)}$. We use $M = 3$ for experiments.

Dropout-based (Gal & Ghahramani, 2016). Dropout-based methods approximate Bayesian inference based on activated dropout layers. It conducts multiple stochastic forward passes with active dropout layers at test time. Similar to Deep ensembles, the entropy of expected softmax probability and variance of multiple predictions are used as aleatoric and epistemic uncertainty scores, respectively. We use $M = 10$ for experiments.

Energy-bounded Learning (EB). For a fair comparison, we also include OOD-exposure for an energy-based model. With the same strategy as Liu et al. (2020), we consider energy-bounded

learning for OOD detection. This approach entails fine-tuning the neural network by assigning lower energy levels to ID data and higher energy levels to OOD data. Specifically, the classification model is trained using the following objective function:

$$\mathcal{L}^{\text{CeEb}} = \mathbb{E}_{(\boldsymbol{X},\boldsymbol{y})\sim\mathcal{D}_{in}^{train}}\mathbb{H}(\boldsymbol{p},\boldsymbol{y}) + \eta \cdot \mathcal{L}^{\text{Eb}} \tag{45}$$

where $\boldsymbol{p}$ is the predicted class probabilities and $\mathcal{L}^{\text{Eb}}$ is the regularization loss defined in terms of energy:

$$\mathcal{L}^{\text{Eb}} = \mathbb{E}_{(\boldsymbol{X}_{in},\boldsymbol{y})\sim\mathcal{D}_{in}^{train}}\left(\max\left(0\ ,\ u_{\boldsymbol{X}_{in}}^{energy} - m_{in}\right)\right)^2 \tag{46}$$

$$= \mathbb{E}_{(\boldsymbol{X}_{out},\boldsymbol{y})\sim\mathcal{D}_{out}^{train}}\left(\max\left(0\ ,\ m_{out} - u_{\boldsymbol{X}_{out}}^{energy}\right)\right)^2 \tag{47}$$

where the m_{in}, m_{out} are two bounded hyperparamters. Details can be found in Liu et al. (2020).

We can also replace cross entropy loss with focal loss for better calibration:

$$\mathcal{L}^{\text{FceEb}} = \mathbb{E}_{(\boldsymbol{X},\boldsymbol{y})\sim\mathcal{D}_{in}^{train}}\text{Focal}(\boldsymbol{p},\boldsymbol{y}) + \eta \cdot \mathcal{L}^{\text{Eb}} \tag{48}$$

where $\text{Focal}(\boldsymbol{p},\boldsymbol{y}) = -\sum_{c=1}^{C} y_c(1-p_c)^{\gamma}\log p_c$.

A.3 Implementation Details

For the model training, we will use equation 49 for the original ENN model optimized by Bayesian loss and equation 50 for our proposed UFCE-based models.

$$\mathcal{L}^{\text{UCE-ENT-ER}} = \mathcal{L}^{\text{UCE-ENT}} + \lambda\mathcal{L}^{\text{ER}} \tag{49}$$

$$\mathcal{L}^{\text{UFCE-ER}} = \mathcal{L}^{\text{UFCE}} + \lambda\mathcal{L}^{\text{ER}} \tag{50}$$

It is important to highlight that $\mathcal{L}^{\text{ER}}$ and $\mathcal{L}^{\text{ENT}}$ represent distinct concepts within our framework. $\mathcal{L}^{\text{ER}}$, identified as a *target loss*, assumes that the level-2 ground truth for pseudo OOD samples corresponds to a flat Dirichlet distribution, reflecting the actual discrepancy between predictions and ground truth. Conversely, $\mathcal{L}^{\text{ENT}}$ is characterized as a *surrogate loss*, fulfilling an auxiliary role. Through the employment of the ENT regularizer, the model is implicitly encouraged to predict a smoother distribution for all training samples.

A.3.1 Hyperparameters

Fixed hyperparamters: We set the weight of the entropy regularization term in the UCE loss (β in Equation 5) to 0.001. The energy-bounded regularization weight in the energy model (η in Equations 46 and 48) is set to 0.0001. For all models where "vehicle" is considered the positive class, we assign a positive class weight of 2. In scenarios where "drivable region" is a positive class, the class weight is set to 1. We employ learning rates of 4×10^{-3} for focal loss variants and 1×10^{-3} for cross-entropy variants, using the Adam optimizer with a weight decay of 1×10^{-7}. The batch size is set to 32 across all experimental scenarios.

Hyperparameters tuning strategy: We tune three regularization weights related to our proposed model: λ, ξ, and γ. Due to computational constraints, we did not perform a full grid search over these hyperparameters. Instead, we conducted a step-by-step search based on the pseudo-OOD detection task, specifically optimizing for the AUPR metric evaluated on the validation set. First, we performed a coarse grid search over $\lambda \in \{0.001, 0.005, 0.01, 0.05, 0.1\}$ with $\xi = 0$ and $\gamma = 0$, finding that $\lambda = 0.01$ generally provided good performance across most scenarios. Next, with λ fixed at 0.01, we tuned $\xi \in \{8, 16, 32, 64, 128\}$ with $\gamma = 0$, and selected $\xi = 64$ for the remaining experiments. Finally, we fine-tuned $\gamma \in \{0.05, 0.5, 1.5\}$ while keeping $\lambda = 0.01$ and $\xi = 64$ fixed. The detailed hyperparameters used in our reported results are listed in Table 6.

Hyperparameters Sensitivity Analysis: To evaluate the robustness of our model with respect to its hyperparameters, we conducted a comprehensive sensitivity analysis on the nuScenes dataset with vehicle segmentation task using the LSS model as the backbone.

Table 6: Hyperparameter Settings for Different Datasets and Methods

Dataset	**Method**	γ	λ	ξ
CARLA	LSS	0.5	0.01	64
	CVT	0.05	0.01	64
	Simple-BEV	0.05	0.01	64
nuScenes	LSS	1	0.01	64
	CVT	0.05	0.01	64
	Simple-BEV	0.05	0.01	64
Lyft	LSS	1	0.01	64
	CVT	0.05	0.01	64
	Simple-BEV	0.05	0.01	64

We first analyze the impact of the hyperparameter λ on model performance, with results presented in Table 7. Intuitively, a larger λ corresponds to a higher pseudo-OOD regularization weight, encouraging the model to predict a uniform Dirichlet distribution for pseudo-OOD pixels. However, this may also negatively affect the original task performance. Experimentally, we observe that larger λ values lead to a decline in pure segmentation and calibration performance. Due to the observed significant variations in segmentation metrics and misclassification results are closely tied to segmentation performance, we ignore the misclassification detection performance here. For OOD detection, we emphasize the AUPR metric as a key indicator. With increasing λ, we initially observe an improvement in AUPR (accompanied by higher AUROC and lower FPR95), followed by a decline as λ becomes too large. This indicates that while moderate pseudo-OOD regularization enhances OOD detection, overly strong regularization can degrade overall performance.

Table 7: Hyperpameter sensitivity analysis for varying λ. We conduct the vehicle segmentation with LSS as the backbone on nuScenes with $\xi = 64$, $\gamma = 0.5$.

λ	Pure Classification		Misclassification			OOD Detection		
	IoU ↑	ECE ↓	AUROC ↑	AUPR ↑	FPR95 ↓	AUROC ↑	AUPR ↑	FPR95 ↓
0.001	0.361	0.00335	0.895	0.320	0.192	0.801	0.224	0.410
0.005	0.357	0.00327	0.890	0.318	0.199	0.833	0.225	0.340
0.01	0.343	0.00035	0.925	0.324	0.191	0.743	0.165	0.383
0.05	0.304	0.01090	0.936	0.300	0.233	0.840	0.115	0.276
0.1	0.259	0.01740	0.919	0.276	0.288	0.860	0.0537	0.230

We then analyze the impact of the hyperparameter γ on model performance, with results presented in Table 8. We observe that varying γ does not significantly affect segmentation performance. However, selecting an appropriate value for γ leads to better calibration performance, as evidenced by the lower Expected Calibration Error (ECE) score, and improved aleatoric uncertainty prediction, indicated by better misclassification detection performance. This demonstrates that the UFCE loss can enhance both calibration and misclassification detection performance. Besides, we observe that OOD detection performance is quite sensitive to the selection of γ.

Table 8: Hyperpameter sensitivity analysis for varying γ. We conduct the vehicle segmentation with LSS as the backbone on nuScenes with $\xi = 0$, $\lambda = 0.1$.

γ	Pure Classification		Misclassification			OOD Detection		
	IoU ↑	ECE↓	AUROC↑	AUPR↑	FPR95↓	AUROC↑	AUPR↑	FPR95↓
0.05	0.349	0.00378	0.913	0.321	0.195	0.876	0.184	0.278
0.5	0.348	0.00166	0.901	0.328	0.187	0.774	0.341	0.358
1.5	0.349	0.01170	0.924	0.331	0.183	0.634	0.334	0.473

Finally, we investigate the effect of hyperparameter ξ on model performance, with results presented in Table 9. First, We observe that increasing ξ led to a slightly higher IoU), indicating improved segmentation accuracy (then we omit the misclassification detection performance considering the correlation between these two tasks). We noted that higher values of ξ resulted in increased AUROC on OOD detection performance in general.

Table 9: Hyperpameter sensitivity analysis for varying ξ. We conduct the vehicle segmentation with LSS as the backbone on nuScenes with $\gamma = 0.5$, $\lambda = 0.01$.

ξ	Pure Classification		Misclassification			OOD Detection		
	IoU ↑	ECE ↓	AUROC ↑	AUPR ↑	FPR95 ↓	AUROC ↑	AUPR ↑	FPR95 ↓
0	0.348	0.00166	0.901	0.328	0.187	0.774	0.341	0.358
8	0.349	0.00079	0.913	0.327	0.186	0.785	0.273	0.348
16	0.351	0.00089	0.910	0.321	0.186	0.747	0.328	0.390
32	0.350	0.00154	0.900	0.324	0.192	0.822	0.321	0.315
64	0.351	0.00133	0.904	0.321	0.187	0.797	0.315	0.364
128	0.353	0.00137	0.893	0.321	0.192	0.818	0.334	0.355

A.4 Dataset Details

Datasets. We consider both synthetic and real-world datasets for our experiments and details are presented in Table 10. For synthetic data, we utilize the widely recognized CARLA simulator (Dosovitskiy et al., 2017) to collect our dataset, which will be made available upon request due to its large size. Our simulated CARLA dataset features five towns with varied layouts and diverse weather conditions to enhance dataset diversity. In terms of real-world data, we employ the nuScenes (Caesar et al., 2020) and Lyft (Kesten et al., 2019) dataset, which is also used in the evaluation of the two segmentation backbones used in our paper: LSS and CVT, as well as an updated leaderboard. We choose not to use the KITTI (Behley et al., 2019) dataset for several reasons. KITTY primarily features suburban streets with low traffic density and simpler traffic scenarios, with annotations limited to the front camera view instead of a full 360-degree perspective. It also lacks radar data and is designated for non-commercial use only. In contrast, nuScenes aims to enhance these features by providing dense data from both urban and suburban environments in Singapore and Boston.

Below, we provide detailed descriptions of each dataset: (1) nuScenes. This dataset comprises of 35661 samples. It offers a 360° view around the ego-vehicle through six camera perspectives, with each view providing both intrinsic and extrinsic details. We resize the camera images to 224x480 pixels, and produce Bird's-Eye-View (BEV) labels of 200x200 pixels for analysis. (2) Lyft. This dataset comprises of 22,888 samples. It offers a 360° view around the ego-vehicle through multiple camera perspectives, providing both intrinsic and extrinsic details for each view. We resize the camera images to 224x480 pixels and generate Bird's-Eye-View (BEV) labels at a resolution of 200x200 pixels for analysis. (3) CARLA. In this simulated environment, six cameras are installed at 60-degree intervals around the ego vehicle, emulating the setup found in nuScenes. The simulation includes various weather conditions (e.g., Clear Noon, Cloudy Noon, Wet Noon) and urban layouts (e.g., Town10, Town03) to enrich the dataset's diversity. For each camera, we capture and record intrinsic and extrinsic information. The dataset consists of 224x480 pixel camera images and 200x200 pixel BEV labels, similar to nuScenes. In total, 40,000 frames are collected for training, with an additional 10,000 frames designated for validation.

Table 10: Dataset details with diversity descriptions.

Dataset	Camera Space			BEV Space			Diversity Description
	Cameras	Positions	Resolution	FOV	Scale	Resolution	
CARLA	6	60-degree intervals around the ego vehicle	224 × 480	90	100 m × 100 m around vehicle	200 × 200	Diverse scenes over 10 weather conditions (e.g., Clear Noon, Cloudy Noon, Wet Noon) and 5 urban layouts (e.g., Town10, Town03)
nuScenes	6	Front, Front-Left, Front-Right, Back-Left, Back-Right, Back	224 × 480	70,110	100 m × 100 m around vehicle, 50 cm resolution	200 × 200	1,000 diverse scenes collected over various weather, time of day, and traffic conditions
Lyft Level 5	6	Front, Front-Left, Front-Right, Side-Left, Side-Right, Back	224 × 480	82	150 m × 150 m around vehicle	Variable	Diverse urban driving scenes with varying traffic densities and environments in Palo Alto, California

True OOD and pseudo OOD setting. We evaluate the quality of the predicted epistemic uncertainty through an out-of-distribution (OOD) detection task. In-Distribution (ID) pixels are those that belong

to the segmentation task with clear labels, such as "vehicle" and "background". **True-OOD** pixels represent a semantic shift from the training data; they only appear in the test dataset and were not seen during training. The OOD detection performance reported in this paper identifies pixels as either ID or true OOD. **Pseudo-OOD** pixels are artificially designated as OOD during training to regularize the model, helping it learn to distinguish between ID and OOD pixels. These pseudo OOD pixels exist in the training and validation sets, and hyperparameter tuning is based on the pseudo-OOD detection performance on the validation set. The detailed setting we used in this paper is presented in Table 11.

Criteria used to select the pseudo-OOD data. We initially adhered to the criteria outlined in the benchmark study by Franchi et al. (2022), a seminal work in the field of autonomous driving, to identify candidate OOD classes. In this context, OOD data typically encompasses less frequently encountered dynamic objects (e.g., motorcycles, bicycles, bears, horses, cows, elephants) and static objects (e.g., food stands, barriers) that are distinct from primary segmentation categories like vehicles, road regions, and pedestrians. These objects were designated as candidate OOD classes. Subsequently, in our experiments, we randomly partitioned these candidate classes into pseudo-OOD and true OOD categories.

It is worth noting that the OOD benchmark dataset MUAD (https://muad-dataset.github.io/) provided by Franchi et al. (2022) was collected using a simulator based on front-camera imagery for image segmentation. However, it does not include a collection of images from multiple cameras or labels for BEV segmentation. To address this, we adopted a similar procedure and generated a BEV segmentation dataset with OOD objects using the well-established CARLA simulator.

Table 11: Dataset configurations for different settings.

Dataset	Setting 1 (Default)			Setting 2			Setting 3		
	ID	Pseudo-OOD	True-OOD	ID	Pseudo-OOD	True-OOD	ID	Pseudo-OOD	True-OOD
CARLA	vehicle	bears, horses, cows, elephants	deer	vehicle	bears, horses, cows, elephants	kangaroo	n.a.	n.a.	n.a.
nuScenes	vehicle	bicycle	motorcycle	vehicle	traffic cones, pushable/pullable objects, motorcycles	barriers	drivable region	bicycle	motorcycle
Lyft	vehicle	bicycle	motorcycle	n.a.	n.a.	n.a.	n.a.	n.a.	n.a.

Splits for evaluation. (1) nuScenes: Considering that only public training and validation sets are available, we report results on the validation set, following standard practice in the literature. Notably, we remove all frames that contain true OOD pixels from both the training and validation sets used for training and evaluation, respectively. For models that are not exposed to pseudo-OOD pixels during training, we also remove frames containing pseudo-OOD objects from the training set. (2) Lyft. We use the same split strategy as nuScenes. (3) CARLA. To introduce pseudo and true OOD objects into our synthetically generated dataset, we employ 3D models of specific objects, integrating these models into the CARLA simulator scenes to generate custom objects. We first gather clean datasets for training, validation, and testing separately, where each frame exclusively contains in-distribution objects. Then, we gather separate train-pseudo and val-pseudo datasets, incorporating pseudo-OOD objects into each scene. Finally, we collect a dataset featuring true OOD objects, specifically deer.

In Table 12, we provide the number of frames and OOD pixel ratio for splitter datasets.

CARLA Data generation process We first introduce key concepts for dataset generation. These are listed from the bottom up in terms of scale to make everything easy to understand. Then we introduce the main control loop.

- Tick: A tick is a single unit of simulation in the simulator. Every tick, the position of vehicles, states of sensors, weather conditions, and traffic lights are updated. A tick is the smallest denomination that we use.
- Frame: A frame is a single sample of data. Each frame consists of 6 RGB images and a single BEV semantic segmentation image. The RGB images have a resolution of 224x480, and the BEV image has a resolution of 200x200. The BEV image covers an area of 100 meters x 100 meters.

Table 12: Dataset split information

Dataset	train	train-aug		val	val-aug		test	
	No. frames	No. frames	Pseudo-OOD ratio	No. frames	No. frames	Pseudo-OOD ratio	No. frames	True-OOD ratio
CARLA	40,000	80,000	0.11%	40,000	80,000	0.14%	2,000	0.07%
nuScenes	19,208	23,831	0.017%	3,878	5,082	0.012%	1,204	0.02%
Lyft	11,487	16,184	0.18%	4,431	6,094	0.016%	113	0.009%

Dataset split principle: "train" and "val" datasets only contain ID pixels, "train-aug" and "val-aug" contain the ID and pseudo-OOD pixels, and "test" set contains both ID and true OOD pixels. For models without pseudo-OOD exposure during training, we use the "train" and "val" datasets. For models with pseudo-OOD exposure, we utilize the "train-aug" and "val-aug" datasets. All models are evaluated on the "test" dataset. When calculating pure segmentation and misclassification performance, we mask out the OOD pixels to focus solely on the ID pixels.

- Scene: We define a scene as a time-frame of N ticks on a specific map. In the beginning of the scene, the map is loaded. Then, 5 vehicles with sensors attached (ego vehicles) are spawned at random locations. These vehicles have 6 RGB cameras attached to them at 60 degree intervals These intervals represent front, front left, front right, back, back let, and back right. We also gather the depth ground truth maps at the same intervals. We place a birds-eye-view segmentation camera above the vehicle that captures an area of 100x100m at a resolution of 200x200 pixels. Then, 50 non-ego vehicles are spawned in random locations. Then, if needed, 40 OOD objects are spawned in random positions. The simulator will run through each of the N ticks one by one in a sequential manner, and will save one frame for each ego vehicle every five ticks.
- Main control loop: The main control loop runs through M scenes, systematically varying weather conditions and urban layouts to generate a diverse dataset.
  - **Weathers Condition**: ClearNoon, CloudyNoon, WetNoon, MidRainyNoon, SoftRainyNoon, ClearSunset, CloudySunset, WetSunset, WetCloudSunset, SoftRainySunset
  - **Urban Layouts**: Town10, Town07, Town05, Town03, Town02. Specifically, we have
    - Town 02: A small simple town with a mixture of residential and commercial buildings.
    - Town 05: Squared-grid town with cross junctions and a bridge. It has multiple lanes per direction. Useful to perform lane changes.
    - Town 07: A rural environment with narrow roads, corn, barns and hardly any traffic lights.
    - Town 10: A downtown urban environment with skyscrapers, residential buildings and an ocean promenade.

  Within each scene:

  - Weather Variation: Every $N/10$ ticks, the weather changes to the next condition in the set. This approach ensures that each weather condition is represented equally throughout the scene.
  - Urban Layout Selection: The town for each scene is selected in a cyclic manner using the following logic: $\texttt{town} = \texttt{towns}[i]; i = (i+1) \mod 5$. where $\texttt{towns}$is the list of urban layouts, and i is the index that cycles through the towns. The modulo operation ensures that after reaching the last town, the index wraps around to the first, providing a continuous loop through the available urban layouts.

  After each scene: All objects are destroyed, and the town environment is cleared. A new scene begins by loading the next town as determined by the selection process. The number of frames can be calculated with $(N/5) * M *$ (No. of ego vehicles).

A.5 Additional Experiments

In this section, we first provide clear definitions and calculations for the evaluation metrics used in our study, ensuring transparency and reproducibility. Then we introduce the additional experimental results.

Pure segmentation via IoU: Intersection over Union (IoU) is used to evaluate the segmentation performance of the models. It is calculated as the IOU for positive class, which is defined as:

$$\text{IoU} = \frac{\text{True Positives}}{\text{True Positives} + \text{False Positives} + \text{False Negatives}}$$

Higher IoU values indicate better segmentation performance, as they reflect accurate predictions for both the object and background regions.

Calibration via ECE: Expected Calibration Error (ECE) measures how well the predicted probabilities align with the true likelihood of correctness. It is computed by dividing the confidence scores into M bins and calculating the weighted average of the difference between accuracy and confidence for each bin:

$$\text{ECE} = \sum_{m=1}^{M} \frac{|B_m|}{n} |\text{acc}(B_m) - \text{conf}(B_m)|$$

where B_m represents the set of predictions in bin m, $|B_m|$ is the number of samples in the bin, n is the total number of samples, $\text{acc}(B_m)$ is the accuracy, and $\text{conf}(B_m)$ is the average confidence. Lower ECE values indicate better calibration. We use $M = 10$ for experiments.

Misclassification detection: To evaluate misclassification detection, we treat misclassified pixels as the positive class and do the binary classification task with the aleatoric uncertainty as the score. Metrics such as Area Under the Receiver Operating Characteristic curve (AUROC) and Area Under the Precision-Recall curve (AUPR) are used.

OOD detection: For out-of-distribution (OOD) detection, we assess the model's ability to differentiate OOD pixels from in-distribution (ID) pixels. Similar to misclassification detection, AUROC and AUPR are used as evaluation metrics, and OOD pixels are positive classes with epistemic uncertainty as the score.

A.5.1 Full Evaluation on Lyft

Results on Lyft dataset. Table 13 presents the comprehensive results on the Lyft (Kesten et al., 2019) dataset using LSS and CVT as model backbones. Our findings on Lyft align with those from our studies on CARLA and nuScenes. Overall, our proposed model employing the UFCE loss consistently outperforms the UCE loss in terms of semantic segmentation accuracy, calibration, and misclassification detection. Furthermore, incorporating epistemic uncertainty scaling and pseudo-OOD exposure significantly enhances OOD detection performance.

A.5.2 Quantitative Evaluation on CALRA (full)

Result on calibration/misclassification detection on CARLA: Table 14 presents the segmentation, calibration, and misclassification detection results on the CARLA dataset using LSS and CVT as model backbones. We observe that our proposed model demonstrates the best OOD detection performance, the second-best calibration performance, and comparable results in segmentation and misclassification detection compared to other models.

A.5.3 Quantitative Evaluation on nuScenes (road segmentation)

Result on OOD detection on nuScenes dataset for road segmentation: Table 15 presents the segmentation and calibration performance on the nuScenes dataset, with "road" designated as the positive class for segmentation. To verify the calibration improvements brought by the proposed UFocal loss, all evaluations are conducted on the clean validation dataset. We observe that our proposed UFocal loss consistently achieves lower ECE and higher IoU scores, indicating better calibration performance and segmentation accuracy compared to the UCE loss. Additionally, the misclassification detection performance is also superior to that of the UCE loss. Compared to other baselines, our model demonstrates top-tier performance.

A.5.4 Quantitative Evaluation on Simple-BEV on nuScenes

Full Results with SimpleBEV backbone on nuScenes dataset for vehicle segmentation. Table 16 presents the full results with the SimpleBEV (Harley et al., 2023) as the backbone. While the original

Table 13: Evaluation on Lyft dataset for vehicle segmentation . Best and Runner-up results are highlighted in red and blue.

Baseline	Loss	LSS						CVT					
		Pure Classification		Misclassification		OOD Detection		Pure Classification		Misclassification		OOD Detection	
		IoU ↑	ECE ↓	AUROC ↑	AUPR ↑	AUROC ↑	AUPR ↑	IoU ↑	ECE ↓	AUROC ↑	AUPR ↑	AUROC ↑	AUPR ↑
Without pseudo OOD													
Entropy	CE	0.405	0.01580	0.875	0.320	0.609	0.002	0.346	0.00723	0.939	0.325	0.805	0.003
	Focal	0.442	0.01350	0.921	0.333	0.691	0.002	0.394	0.00842	0.952	0.345	0.816	0.003
Energy	CE	0.405	0.01580	0.875	0.320	0.609	0.002	0.346	0.00723	0.939	0.325	0.805	0.003
	Focal	0.442	0.01350	0.921	0.333	0.691	0.002	0.394	0.00842	0.952	0.345	0.816	0.003
Ensemble	CE	0.423	0.01020	0.894	0.329	0.403	0.001	0.367	0.00330	0.954	0.327	0.424	0.001
	Focal	0.465	0.00834	0.936	0.333	0.513	0.001	0.429	0.00300	0.962	0.341	0.505	0.001
Dropout	CE	0.392	0.01520	0.867	0.317	0.321	0.001	0.338	0.00761	0.934	0.318	0.396	0.001
	Focal	0.426	0.01320	0.917	0.336	0.365	0.001	0.381	0.00858	0.949	0.347	0.318	0.001
ENN	UCE	0.413	0.00659	0.753	0.234	0.468	0.001	0.358	0.00807	0.887	0.296	0.722	0.002
	UFCE	0.440	0.01110	0.813	0.282	0.532	0.001	0.407	0.00348	0.917	0.342	0.677	0.002
With pseudo OOD													
Energy	CE	0.451	0.01230	0.941	0.345	0.693	0.033	0.402	0.00521	0.960	0.347	0.857	0.021
	Focal	0.481	0.00862	0.960	0.344	0.728	0.034	0.442	0.00149	0.967	0.360	0.850	0.026
ENN	UCE	0.444	0.00615	0.794	0.261	0.876	0.139	0.392	0.00560	0.92	0.324	0.922	0.055
	Ours	0.451	0.00371	0.853	0.301	0.765	0.163	0.437	0.00125	0.938	0.342	0.947	0.120

Observations: 1. The proposed UFCE loss for the ENN model consistently outperforms the commonly used UCE loss across all metrics, showing improvements of 2.6% in segmentation IoU, 0.9 in calibration ECE, 3.9% in misclassification AUROC, and 1.5% in AUPR across LSS and CVT backbone. 2. For road detection, there is no clear evidence showing that Focal loss performs better than classic CE loss in terms of segmentation or aleatoric uncertainty prediction.

Table 14: Calibration and Misclassification detection performance on the CARLA dataset for vehicle segmentation . Best and Runner-up results are highlighted in red and blue.

Model	Loss	LSS					CVT				
		Pure Classification		Misclassification			Pure Classification		Misclassification		
		IoU ↑	ECE↓	AUROC ↑	AUPR ↑	FPR95 ↓	IoU ↑	ECE↓	AUROC ↑	AUPR ↑	FPR95 ↓
Without pseudo OOD											
Entropy	CE	0.403	0.00309	0.928	0.272	0.222	0.361	0.00183	0.952	0.246	0.215
	Focal	0.403	0.00309	0.928	0.272	0.221	0.435	0.00146	0.970	0.265	0.148
Energy	CE	0.403	0.00309	0.928	0.272	0.222	0.361	0.00183	0.952	0.246	0.215
	Focal	0.403	0.00309	0.928	0.272	0.221	0.435	0.00146	0.970	0.265	0.148
Ensemble	CE	0.433	0.00202	0.941	0.266	0.215	0.410	0.00160	0.961	0.222	0.227
	Focal	0.462	0.00140	0.971	0.270	0.157	0.471	0.00135	0.973	0.260	0.154
Dropout	CE	0.409	0.00277	0.922	0.269	0.243	0.366	0.00183	0.944	0.238	0.235
	Focal	0.422	0.00135	0.956	0.293	0.167	0.442	0.00142	0.966	0.264	0.167
ENN	UCE	0.407	0.00212	0.817	0.252	0.345	0.398	0.00098	0.917	0.253	0.192
	UFCE	0.424	0.00033	0.913	0.283	0.153	0.422	0.00103	0.933	0.263	0.154
With pseudo OOD											
Energy	CE	0.441	0.00249	0.975	0.314	0.110	0.425	0.00124	0.977	0.264	0.119
	Focal	0.469	0.00588	0.979	0.277	0.094	0.465	0.00096	0.980	0.266	0.090
ENN	UCE	0.428	0.00131	0.894	0.300	0.193	0.432	0.00457	0.961	0.263	0.133
	Ours	0.459	0.00040	0.950	0.303	0.0989	0.468	0.00180	0.967	0.294	0.097

Observations: 1. Involving pseudo-OOD in the training phase does not impact pure segmentation, calibration and misclassification detection. 2. Without pseudo-OOD, the proposed UFCE loss for the ENN model consistently outperforms the commonly used UCE loss across 9 out of 10 metrics. 3. No single model consistently performs best across all metrics, but Focal consistently performs better than CE.

paper reported a vehicle segmentation IoU of 44.7 on nuScenes, we report 38.2. This discrepancy arises because we adopt a consistent experimental setup across all backbones, including LSS and CVT. Specifically, we exclude frames containing true OOD objects from the training set and use camera images with a resolution of 224×480 without any image augmentations. Additionally, we employ bilinear sampling as the lifting strategy, EfficientNet-B4 as the network backbone, and batch size of 16.

We observe that (1).The proposed model achieves the second-best performance in pure segmentation, with a gap of only 0.1% from the best baseline, while outperforming all models in calibration. (2). All models demonstrate comparable performance in misclassification detection. (3). For OOD detection,

Table 15: Segmentation, Calibration and Misclassification detection on road segmentation for nuScenes. Best and Runner-up results are highlighted in red and blue.

Model	Loss	LSS				CVT			
		Pure Classification		Misclassification		Pure Classification		Misclassification	
		Road IoU↑	ECE↓	AUROC↑	AUPR↑	Road IoU↑	ECE↓	AUROC↑	AUPR↑
Entropy	CE	0.756	0.0448	0.870	0.330	0.637	0.0495	0.835	0.354
	Focal	0.763	0.0266	0.886	0.341	0.678	0.0458	0.848	0.345
Ensemble	CE	0.776	0.0156	0.883	0.309	0.656	0.0269	0.840	0.324
	Focal	0.769	0.0308	0.882	0.314	0.698	0.0263	0.853	0.324
Dropout	CE	0.744	0.0455	0.867	0.329	0.624	0.0573	0.831	0.351
	Focal	0.752	0.0300	0.883	0.337	0.670	0.0511	0.844	0.343
ENN	UCE	0.752	0.0417	0.783	0.291	0.639	0.0455	0.806	0.335
	UFCE	0.760	0.0250	0.839	0.319	0.679	0.0438	0.828	0.336

Observations: 1. The proposed UFCE loss for the ENN model consistently outperforms the commonly used UCE loss across all metrics, showing improvements of 2.6% in segmentation IoU, 0.9 in calibration ECE, 3.9% in misclassification AUROC, and 1.5% in AUPR across LSS and CVT backbone. 2. For road detection, there is no clear evidence showing that Focal loss performs better than classic CE loss in terms of segmentation or aleatoric uncertainty prediction.

the proposed model achieves the best performance in AUROC and AUPR, with a 12% improvement in AUPR over the second-best model and FPR95 is only 0.008 higher than the best baseline.

Table 16: Simple-BEV backbone: Segmentation, Calibration, Misclassification detection, OOD detection performance for vehicle segmentation on nuScenes . Best and Runner-up results are highlighted in red and blue.

model	loss	Pure Classification		Misclassification			OOD Detection		
		IoU ↑	ECE↓	AUROC↑	AUPR↑	FPR95↓	AUROC↑	AUPR↑	FPR95↓
Without pseudo OOD									
Entropy	CE	0.352	0.00721	0.936	0.326	0.196	0.684	0.001	0.816
	Focal	0.366	0.00697	0.942	0.322	0.193	0.661	0.001	0.841
Energy	CE	0.352	0.00721	0.936	0.326	0.196	0.638	0.000	0.819
	Focal	0.366	0.00698	0.942	0.322	0.193	0.614	0.000	0.835
Ensemble	CE	0.373	0.00456	0.946	0.322	0.197	0.534	0.000	0.920
	Focal	0.388	0.00453	0.946	0.322	0.185	0.504	0.000	0.937
Dropout	CE	0.350	0.00617	0.934	0.325	0.207	0.458	0.000	0.964
	Focal	0.364	0.00623	0.940	0.323	0.200	0.523	0.000	0.931
ENN	UCE	0.361	0.00647	0.844	0.285	0.286	0.657	0.000	0.832
	UFCE	0.370	0.00296	0.848	0.294	0.279	0.604	0.000	0.831
With pseudo OOD									
Energy	CE	0.360	0.00586	0.946	0.332	0.183	0.820	0.071	0.326
	Focal	0.372	0.00606	0.947	0.332	0.186	0.838	0.058	0.325
ENN	UCE	0.364	0.00455	0.882	0.314	0.207	0.914	0.215	0.272
	Ours	0.372	0.00315	0.896	0.322	0.187	0.845	0.319	0.356

A.5.5 Robustness on selection of pseudo-OOD

Robustness to the selection of pseudo-OOD (cont.). We investigate how the similarity between pseudo-OOD and true OOD affects epistemic uncertainty predictions. For this, we use two pseudo-OOD and true-OOD pairs for nuScenes and CARLA, with detailed settings presented in Table 11. Generalization results for nuScenes are shown in Table 4, with the main discussion provided in Section 4.2. Generalization results for CARLA are presented in Table 17, where we evaluate OOD detection performance using "kangaroo" as the true OOD and "bears, horses, cows, elephants" as

pseudo-OODs. For this true/pseudo-OOD pair, our proposed framework consistently outperforms others across all six metrics, achieving an average AUPR improvement of 3.2% over the runner-up, sharing the same observation on nuScenes.

Table 17: Robustness Analysis (selection of pseudo-OOD): OOD detection performance for vehicle segmentation on CARLA ("kangaroo" as true OOD). Best and Runner-up results are highlighted in red and blue.

Model	Loss	LSS			CVT		
		AUROC ↑	AUPR ↑	FPR95 ↓	AUROC ↑	AUPR ↑	FPR95 ↓
Without pseudo OOD							
Entropy	CE	0.665	0.005	0.768	0.767	0.007	0.691
	Focal	0.725	0.006	0.727	0.783	0.007	0.675
Energy	CE	0.672	0.005	0.742	0.749	0.006	0.69
	Focal	0.717	0.006	0.726	0.755	0.007	0.675
Ensemble	CE	0.485	0.001	0.963	0.487	0.001	0.962
	Focal	0.449	0.001	0.955	0.504	0.001	0.951
Dropout	CE	0.432	0.001	0.966	0.388	0.001	0.962
	Focal	0.401	0.001	0.967	0.342	0.001	0.974
ENN	UCE	0.623	0.004	0.779	0.68	0.005	0.784
	UFCE	0.593	0.004	0.794	0.727	0.006	0.712
With pseudo OOD							
Energy	CE	0.746	0.045	0.556	0.746	0.034	0.442
	Focal	0.727	0.049	0.489	0.786	0.051	0.425
ENN	UCE	0.818	0.097	0.417	0.911	0.077	0.353
	Ours	0.882	0.111	0.368	0.914	0.127	0.322

Table 18 presents the OOD detection performance across various pseudo/true OOD pairs. The results support our intuition that higher similarity between true and pseudo-OOD pairs leads to improved OOD detection performance, suggesting that identifying representative pseudo-OODs is a promising direction for advancing OOD detection tasks. Notably, our proposed model consistently outperforms the best baseline methods across all eight scenarios, achieving improvements of up to 12.6% in AUPR. This highlights the robustness of our approach, even in settings with less similar OOD pairs.

Table 18: OOD detection performance (AUPR ↑) for similar and dissimilar OOD pairs across datasets and backbones, comparing our model to the best baselines and its ablated variants.

Dataset	Similarity between True/Pseudo OOD	LSS		CVT	
		Best Baseline	Ours	Best Baseline	Ours
nuScenes	Similar	31.5	33.5	21.2	26.9
	Dissimilar	20.8	21.5	11.7	15.3
CARLA	Similar	14.7	20.4	11.1	23.7
	Dissimilar	9.7	11.0	7.7	12.7

A.5.6 Robustness on corrupted dataset

Robustness on nuScenes-C. nuScenes-C(Xie et al., 2024) introduces various corruptions to the validation set of the nuScenes dataset, comprising eight types of corruption, each with three levels of severity: easy, mid, and hard. *Brightness, Dark, Fog, and Snow* represent external environmental dynamics, such as illumination changes or extreme weather conditions. *Motion Blur* and *Color Quant* simulate effects caused by high-speed motion and image quantization, respectively. *Camera Crash* and *Frame Lost* model camera malfunctions.

Using a model trained on the clean nuScenes training dataset (excluding frames containing true OOD pixels), we evaluate its performance on the corrupted validation set to assess its robustness to domain shifts. We compare our model against the most relevant baseline, "ENN-UCE," and the model

that generally performs best in OOD detection tasks, "Energy-Focal". The results are presented in Table 19.

For misclassification detection, our model achieves the highest AUROC in 14 out of 21 scenarios and the second highest in the remaining 7 scenarios. Our model archives the highest AUPR in 13 out of 21 scenarios and the second highest in the remaining 8 scenarios. Our model consistently outperforms the ENN-UCE baseline across all 21 scenarios on both AUROC and AUPR. For OOD detection, our model achieves the best AUPR in 16 out of 21 scenarios and the second-best AUPR for the other 5 scenarios. Our model archives the best AUROC in 8 out of 21 scenarios and second-best in the remaining 13 scenarios. We note that AUROC and AUPR offer different perspectives to measure the quality of a ranking on data points (BEV pixels in our context) for separating positives and negatives. A relatively lower AUROC but higher AUPR for our method in some scenarios suggests our model identifies more true positives among top-ranked pixels than the ENN-UCE model, while ENN-UCE model better separates true positives and negatives among lower-ranked BEV pixels. It indicates that data corruptions in these scenarios may affect the quality of epistemic uncertainty quantification for some lowly ranked pixels, but not for the top ranked ones. However, high AUPR is particularly important in applications where human experts manually verify top-ranked misclassified instances or anomalies. Given the high cost of manual verification, ensuring a high rate of true positives among the top-ranked data points makes AUPR a more suitable metric in such cases.

We observe a greater performance drop under domain shifts with higher corruption severity, consistent with the findings in Xie et al. (2024), where significant performance degradation was noted in the segmentation task using CVT on nuScenes compared to the clean dataset. Additionally, sensor-driven distortions, such as color quantization and motion blur, have the least impact, while snow and camera crashes cause the most severe performance degradation. These experiments highlight the need for robust models or optimization strategies, which we plan to explore as a future direction.

A.5.7 Robustness on diverse conditions (CARLA)

We evaluate our models on diverse subsets of the test sets, considering variations in urban layouts and weather conditions. In the CARLA dataset, we include four towns across 10 weather conditions, with details on dataset generation provided in Appendix A.4.

Evaluation results on different towns are shown in Table 20. Towns 2 and 5 represent denser urban layouts compared to Towns 7 and 10. We observe consistent performance across each subset, aligning with the evaluations conducted on the full CARLA dataset. Specifically, our model consistently outperforms all baselines in OOD detection tasks across all towns, while also achieving better segmentation, calibration, and misclassification detection compared to the standard UCE loss. Furthermore, we observe performance gaps across urban layouts, highlighting the need to improve model robustness in diverse environments.

Evaluation results on varying weather conditions are shown in table 21, 22, 23. While the results align with the conclusions drawn from evaluations on the full dataset when comparing our proposed model to the baselines, we also observe performance variations across different weather conditions. Interestingly, the results challenge the intuition that the best performance would occur under "ClearNoon" conditions. Notably, OOD detection performance is positively correlated with segmentation performance, which may be attributed to clearer environments improving segmentation quality and, consequently, OOD detection.

A.5.8 Robustness on model initializations

We report the model variance for our proposed model in Table 24 and the evidential UCE baseline. We randomly initialize the model three times and the variance is within 3%.

A.5.9 Qualitative Evaluations for model comparison

We qualitatively analyze the model performance with pixel-level prediction when viewed from a bird's eye perspective, and show the effectiveness of our proposed model.

We first present the semantic segmentation predictions in Figure 4. Our model demonstrates comparable segmentation performance to energy-based, dropout, and ensemble models. Compared to ENN-UCE, our model produces tighter object boundary predictions.

Table 19: Robustness Analysis (data corruption): evaluation on estimated uncertainty with CVT as the backbone on nuScenes-C.

Corruption Type	Severity	Model	Misclassification			OOD Detection		
			AUROC ↑	AUPR ↑	FPR95 ↓	AUROC ↑	AUPR ↑	FPR95 ↓
None	Clean	Energy-Focal	0.955	0.321	0.196	0.860	0.024	0.319
		ENN-UCE	0.919	0.313	0.227	0.921	0.212	0.306
		Ours	0.934	0.321	0.196	0.928	0.269	0.244
CameraCrash	Easy	Energy-Focal	0.863	0.226	0.436	0.710	0.016	0.581
		ENN-UCE	0.823	0.195	0.478	0.859	0.052	0.459
		Ours	0.878	0.318	0.365	0.787	0.109	0.525
	Mid	Energy-Focal	0.785	0.140	0.644	0.615	0.011	0.742
		ENN-UCE	0.727	0.117	0.659	0.723	0.008	0.734
		Ours	0.867	0.351	0.538	0.651	0.067	0.700
	Hard	Energy-Focal	0.796	0.151	0.605	0.623	0.004	0.809
		ENN-UCE	0.751	0.140	0.611	0.791	0.003	0.756
		Ours	0.813	0.251	0.440	0.663	0.027	0.773
FrameLost	Easy	Energy-Focal	0.880	0.235	0.411	0.712	0.021	0.536
		ENN-UCE	0.846	0.227	0.423	0.862	0.118	0.483
		Ours	0.880	0.291	0.364	0.805	0.148	0.533
	Mid	Energy-Focal	0.783	0.132	0.654	0.516	0.003	0.792
		ENN-UCE	0.727	0.117	0.673	0.743	0.044	0.790
		Ours	0.848	0.290	0.503	0.605	0.038	0.843
	Hard	Energy-Focal	0.728	0.112	0.723	0.499	0.002	0.871
		ENN-UCE	0.657	0.074	0.785	0.674	0.032	0.799
		Ours	0.826	0.280	0.572	0.559	0.024	0.898
ColorQuant	Easy	Energy-Focal	0.949	0.315	0.209	0.850	0.025	0.354
		ENN-UCE	0.905	0.307	0.246	0.926	0.174	0.301
		Ours	0.925	0.310	0.219	0.923	0.243	0.275
	Mid	Energy-Focal	0.929	0.297	0.263	0.825	0.028	0.407
		ENN-UCE	0.866	0.273	0.302	0.915	0.100	0.322
		Ours	0.902	0.287	0.289	0.889	0.144	0.367
	Hard	Energy-Focal	0.866	0.223	0.436	0.777	0.025	0.579
		ENN-UCE	0.775	0.197	0.462	0.843	0.008	0.507
		Ours	0.831	0.227	0.445	0.866	0.008	0.431
MotionBlur	Easy	Energy-Focal	0.947	0.309	0.229	0.831	0.024	0.357
		ENN-UCE	0.899	0.284	0.279	0.921	0.194	0.384
		Ours	0.934	0.307	0.228	0.931	0.244	0.266
	Mid	Energy-Focal	0.900	0.249	0.374	0.748	0.020	0.573
		ENN-UCE	0.820	0.225	0.387	0.853	0.149	0.443
		Ours	0.898	0.260	0.342	0.857	0.155	0.417
	Hard	Energy-Focal	0.864	0.214	0.443	0.739	0.020	0.616
		ENN-UCE	0.772	0.195	0.451	0.836	0.138	0.494
		Ours	0.867	0.235	0.402	0.833	0.131	0.463
Brightness	Easy	Energy-Focal	0.939	0.300	0.253	0.875	0.049	0.314
		ENN-UCE	0.881	0.278	0.278	0.915	0.176	0.346
		Ours	0.911	0.288	0.254	0.898	0.172	0.329
	Mid	Energy-Focal	0.909	0.261	0.342	0.852	0.038	0.375
		ENN-UCE	0.833	0.227	0.379	0.860	0.057	0.434
		Ours	0.881	0.248	0.360	0.883	0.075	0.324
	Hard	Energy-Focal	0.887	0.239	0.400	0.803	0.008	0.461
		ENN-UCE	0.792	0.202	0.448	0.792	0.010	0.494
		Ours	0.862	0.221	0.442	0.870	0.037	0.420
Snow	Easy	Energy-Focal	0.890	0.233	0.387	0.809	0.017	0.619
		ENN-UCE	0.741	0.183	0.482	0.750	0.057	0.600
		Ours	0.841	0.237	0.384	0.830	0.104	0.480
	Mid	Energy-Focal	0.839	0.169	0.523	0.785	0.006	0.636
		ENN-UCE	0.613	0.080	0.732	0.679	0.004	0.762
		Ours	0.798	0.176	0.512	0.724	0.053	0.626
	Hard	Energy-Focal	0.826	0.158	0.547	0.792	0.005	0.685
		ENN-UCE	0.580	0.063	0.797	0.604	0.001	0.809
		Ours	0.754	0.137	0.604	0.676	0.067	0.709
Fog	Easy	Energy-Focal	0.920	0.280	0.310	0.873	0.029	0.341
		ENN-UCE	0.857	0.249	0.352	0.840	0.134	0.485
		Ours	0.906	0.271	0.318	0.880	0.173	0.353
	Mid	Energy-Focal	0.899	0.250	0.376	0.849	0.019	0.416
		ENN-UCE	0.858	0.248	0.372	0.829	0.114	0.498
		Ours	0.892	0.251	0.368	0.856	0.160	0.426
	Hard	Energy-Focal	0.878	0.227	0.426	0.803	0.014	0.427
		ENN-UCE	0.851	0.239	0.395	0.838	0.061	0.500
		Ours	0.890	0.241	0.388	0.823	0.090	0.432

Table 20: Robustness Analysis (urban layouts): evaluation with LSS backbone on CARLA in diverse towns. Best results are highlighted in red.

pseudo OOD	model	loss	Pure Classification		Misclassification			OOD Detection		
			IoU ↑	ECE↓	AUROC↑	AUPR↑	FPR95↓	AUROC↑	AUPR↑	FPR95↓
Town 10										
No	Baseline	CE	0.377	0.00331	0.931	0.270	0.228	0.688	0.003	0.805
		Focal	0.392	0.00140	0.956	0.291	0.177	0.755	0.003	0.749
	Energy	CE	0.377	0.00331	0.931	0.270	0.228	0.667	0.002	0.784
		Focal	0.392	0.00140	0.956	0.291	0.177	0.748	0.003	0.754
	Ensemble	CE	0.409	0.00218	0.942	0.257	0.228	0.491	0.001	0.963
		Focal	0.431	0.00165	0.964	0.262	0.194	0.453	0.001	0.961
	Dropout	CE	0.381	0.00299	0.921	0.264	0.252	0.462	0.001	0.960
		Focal	0.398	0.00151	0.941	0.276	0.213	0.391	0.001	0.967
	Evidential	UCE	0.384	0.00231	0.813	0.245	0.352	0.604	0.002	0.816
		UFCE	0.390	0.00031	0.905	0.274	0.167	0.578	0.003	0.820
Yes	Energy	CE	0.413	0.00263	0.969	0.297	0.141	0.857	0.058	0.358
		Focal	0.427	0.00586	0.976	0.278	0.111	0.861	0.061	0.284
	Evidential	UCE	0.403	0.00141	0.876	0.276	0.228	0.866	0.106	0.338
		Ours	0.427	0.00064	0.939	0.286	0.133	0.946	0.180	0.235
Town 5										
No	Baseline	CE	0.407	0.00329	0.930	0.289	0.208	0.677	0.003	0.784
		Focal	0.414	0.00158	0.960	0.303	0.158	0.765	0.003	0.729
	Energy	CE	0.407	0.00329	0.930	0.289	0.208	0.678	0.003	0.763
		Focal	0.414	0.00158	0.960	0.303	0.158	0.766	0.003	0.719
	Ensemble	CE	0.438	0.00207	0.942	0.278	0.201	0.493	0.001	0.961
		Focal	0.457	0.00139	0.969	0.283	0.158	0.442	0.001	0.960
	Dropout	CE	0.413	0.00294	0.919	0.276	0.235	0.437	0.001	0.963
		Focal	0.420	0.00170	0.948	0.291	0.186	0.401	0.001	0.964
	Evidential	UCE	0.413	0.00229	0.822	0.256	0.334	0.630	0.002	0.798
		UFCE	0.416	0.00007	0.916	0.291	0.147	0.520	0.002	0.832
Yes	Energy	CE	0.443	0.00267	0.975	0.315	0.117	0.878	0.071	0.298
		Focal	0.456	0.00609	0.979	0.282	0.106	0.892	0.086	0.214
	Evidential	UCE	0.441	0.00136	0.893	0.294	0.196	0.891	0.144	0.256
		Ours	0.455	0.00049	0.945	0.306	0.111	0.957	0.213	0.192
Town 7										
No	Baseline	CE	0.376	0.00348	0.935	0.283	0.206	0.599	0.001	0.877
		Focal	0.393	0.00182	0.967	0.311	0.126	0.725	0.002	0.821
	Energy	CE	0.376	0.00348	0.935	0.283	0.206	0.604	0.001	0.849
		Focal	0.393	0.00182	0.967	0.311	0.126	0.706	0.002	0.820
	Ensemble	CE	0.400	0.00224	0.951	0.276	0.181	0.482	0.001	0.953
		Focal	0.425	0.00132	0.975	0.295	0.134	0.460	0.001	0.957
	Dropout	CE	0.374	0.00322	0.929	0.279	0.225	0.509	0.001	0.951
		Focal	0.387	0.00182	0.960	0.308	0.149	0.461	0.001	0.952
	Evidential	UCE	0.384	0.00244	0.822	0.259	0.333	0.532	0.001	0.868
		UFCE	0.394	0.00017	0.922	0.304	0.136	0.550	0.001	0.839
Yes	Energy	CE	0.418	0.00282	0.975	0.325	0.097	0.845	0.059	0.349
		Focal	0.420	0.00478	0.982	0.311	0.078	0.888	0.076	0.236
	Evidential	UCE	0.410	0.00156	0.899	0.308	0.184	0.858	0.126	0.326
		Ours	0.438	0.00035	0.957	0.320	0.079	0.949	0.230	0.227
Town 2										
No	Baseline	CE	0.407	0.00320	0.943	0.294	0.185	0.696	0.002	0.788
		Focal	0.437	0.00115	0.971	0.310	0.114	0.759	0.002	0.754
	Energy	CE	0.407	0.00320	0.943	0.294	0.185	0.697	0.002	0.753
		Focal	0.437	0.00115	0.971	0.310	0.114	0.757	0.002	0.750
	Ensemble	CE	0.445	0.00195	0.954	0.287	0.174	0.490	0.001	0.964
		Focal	0.478	0.00125	0.978	0.292	0.117	0.461	0.001	0.954
	Dropout	CE	0.411	0.00291	0.935	0.287	0.204	0.436	0.001	0.967
		Focal	0.440	0.00133	0.964	0.299	0.136	0.397	0.001	0.962
	Evidential	UCE	0.422	0.00203	0.842	0.275	0.297	0.632	0.002	0.800
		UFCE	0.435	0.00029	0.925	0.306	0.130	0.540	0.001	0.870
Yes	Energy	CE	0.458	0.00246	0.979	0.321	0.101	0.894	0.057	0.261
		Focal	0.473	0.00571	0.985	0.308	0.067	0.893	0.062	0.225
	Evidential	UCE	0.444	0.00114	0.907	0.309	0.168	0.896	0.093	0.271
		Ours	0.479	0.00022	0.963	0.319	0.074	0.964	0.156	0.161

Table 21: Robustness Analysis (weather conditions - part 1): evaluation with LSS backbone on CARLA in diverse weather conditions. Best results are highlighted in red.

pseudo OOD	model	loss	Pure Classification		Misclassification			OOD Detection		
			IoU ↑	ECE↓	AUROC↑	AUPR↑	FPR95↓	AUROC↑	AUPR↑	FPR95↓
ClearNoon										
No	Baseline	CE	0.401	0.00318	0.927	0.275	0.217	0.654	0.002	0.839
		Focal	0.420	0.00159	0.959	0.295	0.156	0.737	0.002	0.761
	Energy	CE	0.401	0.00318	0.927	0.275	0.217	0.648	0.002	0.809
		Focal	0.420	0.00159	0.959	0.296	0.156	0.740	0.002	0.757
	Ensemble	CE	0.433	0.00207	0.941	0.261	0.200	0.493	0.001	0.958
		Focal	0.460	0.00146	0.969	0.271	0.160	0.454	0.001	0.953
	Dropout	CE	0.398	0.00292	0.920	0.270	0.235	0.484	0.001	0.947
		Focal	0.419	0.00154	0.952	0.289	0.178	0.411	0.001	0.957
	Evidential	UCE	0.411	0.00220	0.815	0.244	0.348	0.573	0.002	0.831
		UFCE	0.416	0.00015	0.912	0.287	0.157	0.543	0.002	0.834
Yes	Energy	CE	0.449	0.00255	0.975	0.317	0.111	0.852	0.051	0.347
		Focal	0.449	0.00493	0.980	0.299	0.087	0.862	0.064	0.278
	Evidential	UCE	0.443	0.00133	0.889	0.292	0.203	0.866	0.098	0.299
		Ours	0.455	0.00038	0.950	0.310	0.091	0.945	0.159	0.255
CloudyNoon										
No	Baseline	CE	0.434	0.00300	0.926	0.278	0.213	0.679	0.002	0.801
		Focal	0.428	0.00136	0.969	0.307	0.130	0.731	0.002	0.760
	Energy	CE	0.387	0.00343	0.940	0.284	0.206	0.664	0.002	0.783
		Focal	0.413	0.00133	0.963	0.300	0.145	0.731	0.002	0.764
	Ensemble	CE	0.419	0.00219	0.947	0.277	0.202	0.507	0.001	0.948
		Focal	0.460	0.00118	0.975	0.304	0.132	0.463	0.001	0.956
	Dropout	CE	0.415	0.00290	0.933	0.286	0.220	0.485	0.001	0.959
		Focal	0.417	0.00163	0.955	0.303	0.164	0.428	0.001	0.951
	Evidential	UCE	0.418	0.00222	0.833	0.273	0.313	0.587	0.002	0.836
		UFCE	0.423	0.00016	0.923	0.307	0.136	0.560	0.002	0.833
Yes	Energy	CE	0.454	0.00256	0.981	0.331	0.082	0.913	0.068	0.231
		Focal	0.487	0.00415	0.985	0.306	0.070	0.922	0.090	0.158
	Evidential	UCE	0.451	0.00120	0.913	0.316	0.158	0.897	0.124	0.236
		Ours	0.471	0.00010	0.965	0.332	0.059	0.975	0.229	0.104
WetNoon										
No	Baseline	CE	0.415	0.00316	0.940	0.294	0.189	0.643	0.002	0.832
		Focal	0.418	0.00159	0.967	0.319	0.128	0.754	0.003	0.739
	Energy	CE	0.415	0.00316	0.940	0.294	0.189	0.654	0.002	0.799
		Focal	0.418	0.00159	0.967	0.319	0.128	0.755	0.003	0.739
	Ensemble	CE	0.439	0.00199	0.956	0.300	0.162	0.501	0.001	0.954
		Focal	0.460	0.00118	0.975	0.303	0.132	0.463	0.001	0.957
	Dropout	CE	0.415	0.00290	0.933	0.286	0.220	0.485	0.001	0.959
		Focal	0.417	0.00163	0.955	0.303	0.164	0.428	0.001	0.951
	Evidential	UCE	0.418	0.00222	0.833	0.272	0.313	0.587	0.002	0.835
		UFCE	0.423	0.00015	0.923	0.307	0.136	0.560	0.002	0.833
Yes	Energy	CE	0.454	0.00256	0.981	0.330	0.082	0.913	0.068	0.231
		Focal	0.467	0.00549	0.987	0.308	0.052	0.911	0.078	0.177
	Evidential	UCE	0.451	0.00120	0.913	0.317	0.158	0.897	0.124	0.236
		Ours	0.471	0.00010	0.965	0.333	0.059	0.975	0.229	0.104
MidRainyNoon										
No	Baseline	CE	0.410	0.00319	0.938	0.302	0.192	0.657	0.002	0.838
		Focal	0.428	0.00136	0.969	0.306	0.130	0.731	0.002	0.760
	Energy	CE	0.410	0.00319	0.938	0.302	0.192	0.672	0.002	0.798
		Focal	0.428	0.00135	0.969	0.306	0.130	0.735	0.002	0.765
	Ensemble	CE	0.445	0.00196	0.953	0.283	0.173	0.474	0.001	0.969
		Focal	0.466	0.00129	0.978	0.297	0.121	0.457	0.001	0.963
	Dropout	CE	0.418	0.00283	0.927	0.286	0.220	0.475	0.001	0.957
		Focal	0.432	0.00142	0.956	0.296	0.167	0.442	0.001	0.955
	Evidential	UCE	0.420	0.00211	0.834	0.264	0.311	0.595	0.002	0.817
		UFCE	0.429	0.00014	0.926	0.297	0.128	0.515	0.001	0.871
Yes	Energy	CE	0.453	0.00255	0.981	0.327	0.083	0.904	0.085	0.249
		Focal	0.462	0.00564	0.986	0.308	0.058	0.909	0.089	0.189
	Evidential	UCE	0.447	0.00118	0.910	0.310	0.164	0.901	0.143	0.259
		Ours	0.469	0.00034	0.963	0.312	0.068	0.965	0.268	0.148

Table 22: Robustness Analysis (weather conditions - part 2): evaluation with LSS backbone on CARLA in diverse weather conditions. Best results are highlighted in red.

pseudo OOD	model	loss	Pure Classification		Misclassification			OOD Detection		
			IoU ↑	ECE↓	AUROC↑	AUPR↑	FPR95↓	AUROC↑	AUPR↑	FPR95↓
SoftRainNoon										
No	Baseline	CE	0.395	0.00333	0.942	0.293	0.197	0.655	0.002	0.842
		Focal	0.413	0.00133	0.963	0.299	0.145	0.734	0.002	0.758
	Energy	CE	0.387	0.00343	0.940	0.284	0.206	0.664	0.002	0.783
		Focal	0.413	0.00133	0.963	0.300	0.145	0.731	0.002	0.764
	Ensemble	CE	0.439	0.00199	0.956	0.300	0.162	0.501	0.001	0.954
		Focal	0.460	0.00118	0.975	0.303	0.132	0.462	0.001	0.957
	Dropout	CE	0.415	0.00290	0.933	0.286	0.220	0.485	0.001	0.959
		Focal	0.417	0.00163	0.955	0.303	0.164	0.428	0.001	0.951
	Evidential	UCE	0.418	0.00222	0.833	0.272	0.313	0.587	0.002	0.836
		UFCE	0.423	0.00016	0.923	0.308	0.136	0.560	0.002	0.833
Yes	Energy	CE	0.454	0.00256	0.981	0.330	0.082	0.913	0.068	0.231
		Focal	0.441	0.00603	0.983	0.297	0.076	0.902	0.071	0.209
	Evidential	UCE	0.451	0.00120	0.913	0.317	0.158	0.897	0.124	0.236
		Ours	0.471	0.00010	0.965	0.332	0.059	0.975	0.229	0.104
ClearSunset										
No	Baseline	CE	0.387	0.00343	0.940	0.283	0.206	0.668	0.002	0.804
		Focal	0.413	0.00134	0.963	0.300	0.145	0.734	0.002	0.758
	Energy	CE	0.387	0.00343	0.940	0.283	0.206	0.664	0.002	0.783
		Focal	0.418	0.00159	0.967	0.318	0.128	0.755	0.003	0.739
	Ensemble	CE	0.439	0.00199	0.956	0.300	0.162	0.501	0.001	0.954
		Focal	0.460	0.00118	0.975	0.303	0.132	0.463	0.001	0.956
	Dropout	CE	0.415	0.00290	0.933	0.286	0.220	0.485	0.001	0.959
		Focal	0.417	0.00163	0.955	0.303	0.164	0.428	0.001	0.951
	Evidential	UCE	0.418	0.00222	0.833	0.272	0.313	0.587	0.002	0.835
		UFCE	0.423	0.00015	0.923	0.307	0.136	0.560	0.002	0.833
Yes	Energy	CE	0.454	0.00256	0.981	0.330	0.082	0.913	0.068	0.231
		Focal	0.445	0.00588	0.977	0.278	0.106	0.868	0.073	0.261
	Evidential	UCE	0.451	0.00120	0.913	0.316	0.158	0.897	0.124	0.236
		Ours	0.471	0.00010	0.965	0.333	0.059	0.975	0.229	0.104
CloudySunset										
No	Baseline	CE	0.374	0.00349	0.933	0.281	0.218	0.678	0.002	0.790
		Focal	0.380	0.00145	0.966	0.307	0.143	0.771	0.003	0.771
	Energy	CE	0.373	0.00342	0.938	0.279	0.209	0.658	0.002	0.799
		Focal	0.391	0.00133	0.966	0.300	0.141	0.766	0.003	0.717
	Ensemble	CE	0.401	0.00215	0.950	0.277	0.190	0.489	0.001	0.957
		Focal	0.427	0.00143	0.973	0.282	0.157	0.425	0.001	0.964
	Dropout	CE	0.376	0.00317	0.930	0.267	0.235	0.448	0.001	0.959
		Focal	0.398	0.00162	0.953	0.289	0.176	0.383	0.001	0.952
	Evidential	UCE	0.370	0.00246	0.834	0.265	0.310	0.612	0.002	0.791
		UFCE	0.387	0.00030	0.919	0.298	0.148	0.538	0.002	0.803
Yes	Energy	CE	0.404	0.00277	0.974	0.319	0.121	0.865	0.059	0.318
		Focal	0.427	0.00613	0.979	0.289	0.113	0.889	0.065	0.213
	Evidential	UCE	0.401	0.00147	0.885	0.288	0.209	0.871	0.104	0.328
		Ours	0.431	0.00062	0.947	0.297	0.117	0.959	0.182	0.217
WetSunset										
No	Baseline	CE	0.371	0.00344	0.933	0.283	0.213	0.684	0.002	0.780
		Focal	0.391	0.00133	0.966	0.299	0.141	0.772	0.003	0.717
	Energy	CE	0.373	0.00342	0.938	0.278	0.209	0.658	0.002	0.799
		Focal	0.391	0.00133	0.966	0.299	0.141	0.766	0.003	0.717
	Ensemble	CE	0.402	0.00214	0.950	0.277	0.190	0.489	0.001	0.957
		Focal	0.427	0.00143	0.973	0.282	0.157	0.425	0.001	0.964
	Dropout	CE	0.376	0.00317	0.930	0.267	0.235	0.448	0.001	0.960
		Focal	0.398	0.00162	0.953	0.289	0.176	0.383	0.001	0.953
	Evidential	UCE	0.370	0.00246	0.834	0.265	0.310	0.612	0.002	0.791
		UFCE	0.387	0.00030	0.919	0.299	0.148	0.538	0.002	0.803
Yes	Energy	CE	0.404	0.00277	0.974	0.319	0.121	0.865	0.059	0.318
		Focal	0.427	0.00613	0.979	0.288	0.113	0.889	0.065	0.213
	Evidential	UCE	0.401	0.00147	0.885	0.288	0.209	0.871	0.104	0.328
		Ours	0.431	0.00062	0.947	0.296	0.117	0.959	0.182	0.217

Table 23: Robustness Analysis (weather conditions - part 3): evaluation with LSS backbone on CARLA in diverse weather conditions. Best results are highlighted in red.

pseudo OOD	model	loss	Pure Classification		Misclassification			OOD Detection		
			IoU ↑	ECE↓	AUROC↑	AUPR↑	FPR95↓	AUROC↑	AUPR↑	FPR95↓
WetCloudySunset										
No	Baseline	CE	0.361	0.00353	0.932	0.279	0.214	0.680	0.002	0.788
		Focal	0.391	0.00133	0.966	0.299	0.141	0.772	0.003	0.718
	Energy	CE	0.373	0.00342	0.938	0.279	0.209	0.658	0.002	0.799
		Focal	0.391	0.00133	0.966	0.299	0.141	0.766	0.003	0.717
	Ensemble	CE	0.401	0.00215	0.950	0.277	0.190	0.489	0.001	0.957
		Focal	0.427	0.00143	0.973	0.281	0.157	0.425	0.001	0.964
	Dropout	CE	0.376	0.00317	0.930	0.267	0.235	0.448	0.001	0.960
		Focal	0.398	0.00162	0.953	0.289	0.176	0.383	0.001	0.953
	Evidential	UCE	0.370	0.00246	0.834	0.266	0.310	0.612	0.002	0.791
		UFCE	0.387	0.00030	0.920	0.299	0.148	0.538	0.002	0.803
Yes	Energy	CE	0.404	0.00277	0.974	0.319	0.121	0.865	0.059	0.318
		Focal	0.427	0.00613	0.979	0.288	0.113	0.889	0.065	0.213
	Evidential	UCE	0.401	0.00147	0.885	0.288	0.209	0.871	0.104	0.328
		Ours	0.431	0.00062	0.947	0.297	0.117	0.959	0.182	0.217
SoftRainSunset										
No	Baseline	CE	0.373	0.00342	0.938	0.279	0.209	0.681	0.002	0.810
		Focal	0.448	0.00170	0.958	0.313	0.141	0.737	0.003	0.711
	Energy	CE	0.434	0.00300	0.926	0.277	0.213	0.674	0.002	0.770
		Focal	0.448	0.00170	0.958	0.313	0.141	0.736	0.003	0.708
	Ensemble	CE	0.463	0.00194	0.944	0.276	0.187	0.504	0.001	0.958
		Focal	0.490	0.00127	0.970	0.292	0.144	0.463	0.001	0.960
	Dropout	CE	0.431	0.00272	0.924	0.277	0.219	0.478	0.001	0.955
		Focal	0.442	0.00140	0.952	0.311	0.154	0.428	0.001	0.953
	Evidential	UCE	0.443	0.00206	0.816	0.258	0.347	0.595	0.002	0.806
		UFCE	0.441	0.00025	0.914	0.301	0.153	0.553	0.002	0.826
Yes	Energy	CE	0.490	0.00238	0.979	0.324	0.084	0.906	0.072	0.250
		Focal	0.487	0.00415	0.985	0.305	0.070	0.922	0.090	0.158
	Evidential	UCE	0.482	0.00112	0.893	0.306	0.197	0.913	0.170	0.195
		Ours	0.494	0.00029	0.956	0.325	0.072	0.975	0.276	0.105

Table 24: Variance for CVT on nuScenes.

Num. Models	Model	Pure Classification		Misclassification		OOD	
		IoU ↑	ECE ↓	AUROC ↑	AUPR ↑	AUROC ↑	AUPR ↑
3	UFCE-EUS-ER	34.4 ± 0.0013	0.0793 ± 0.000016	94.4 ± 0.0009	32.8 ± 0.0021	92.4 ± 0.021	28.7 ± 0.29
	UCE-ENT-EUS-ER	31.3 ± 0.00053	0.353 ± 0.00000511	92.7 ± 0.0000023	31.8 ± 0.001	87.5 ± 0.31	25.4 ± 0.00063

Figure 4: Comparison of Semantic Segmentation Performance: Each row represents an example, with the first column showing the ground truth labels, where the yellow regions indicate the positive class ("vehicle" in these examples). We visualize the predicted probabilities for the positive class generated by our model and four baselines. Brighter regions correspond to higher probability values.

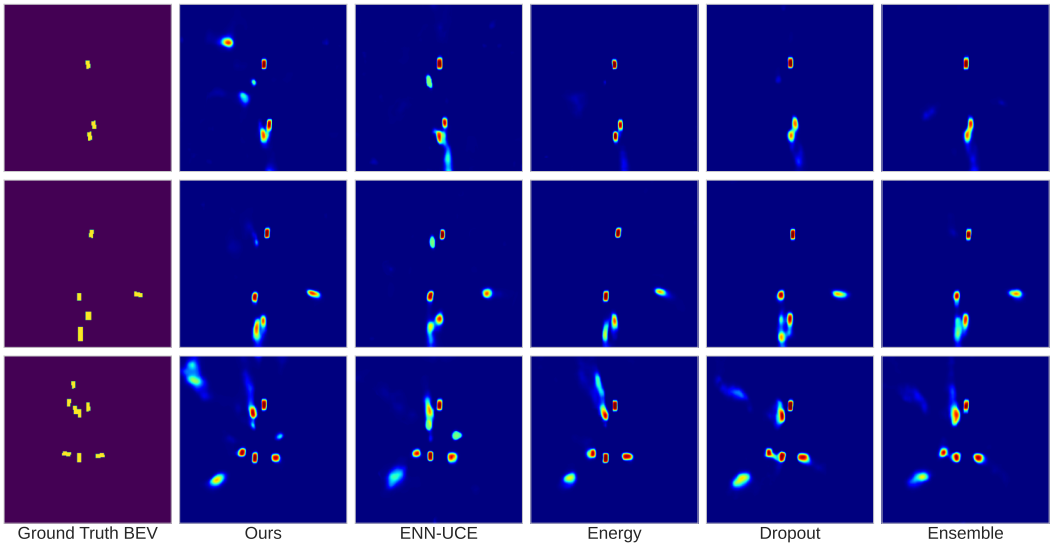

We present the predicted aleatoric uncertainty in Figure 5. We anticipate that correctly classified pixels will exhibit low aleatoric uncertainty, while misclassified pixels will display high aleatoric uncertainty. Analyzing misclassification detection is complex because the ground truth varies across different model predictions. Based on these three frames, we cannot see a large performance difference between the various model variants.

Figure 5: Comparison of Predicted Aleatoric Uncertainty for Misclassification Detection: Each row represents an example, with each pair of columns corresponding to one model. The left column shows the misclassified labels, where yellow indicates misclassified pixels, while the right column visualizes the predicted aleatoric uncertainty for the same model, with brighter regions representing higher uncertainty values.

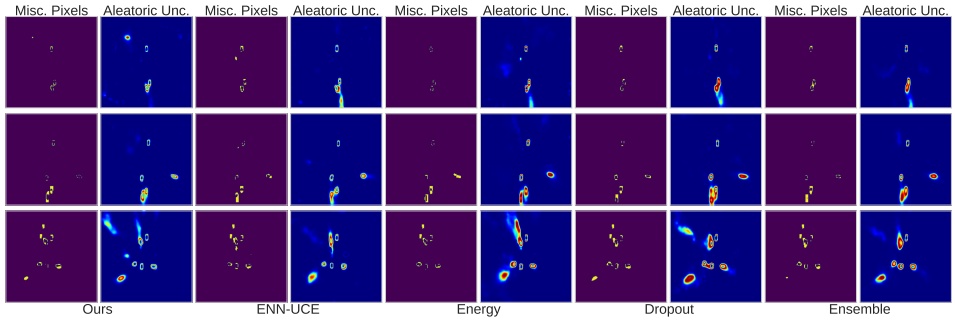

Figure 6 presents the predicted epistemic uncertainty. Ideally, in-distribution (ID) pixels should exhibit low epistemic uncertainty, while out-of-distribution (OOD) pixels should show high uncertainty.

Our focus is on the relative uncertainty levels between ID and OOD pixels rather than the absolute uncertainty scale. The results demonstrate that our proposed model achieves the most accurate identification of OOD pixels, indicating the best-predicted epistemic uncertainties. In contrast, the ENN-UCE baseline shows a significant increase in false positives. Even with the assistance of pseudo-OOD, the energy model fails to accurately locate OOD pixels. Dropout and ensemble models, unable to leverage pseudo-OOD, exhibit the worst performance.

Figure 6: Comparison of Predicted Epistemic Uncertainty for OOD Detection: Each row represents an example, with the first column displaying the ground truth labels, where yellow regions indicate OOD pixels ("motorcycle" in these examples). The predicted epistemic uncertainty is visualized, with brighter regions indicating higher uncertainty values.